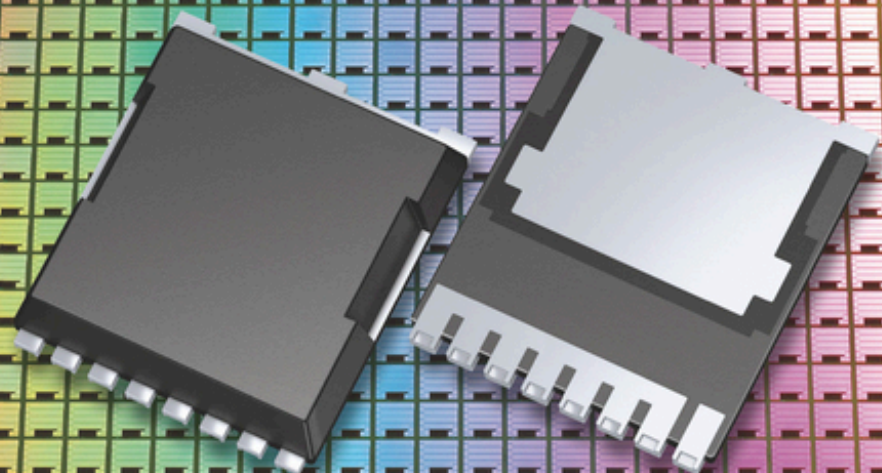


Edited by Peter Wellmann, Noboru Ohtani,  
and Roland Rupp

# Wide Bandgap Semiconductors for Power Electronics

Materials, Devices, Applications





## **Wide Bandgap Semiconductors for Power Electronics**



# **Wide Bandgap Semiconductors for Power Electronics**

Materials, Devices, Applications

*Volume 1*

*Edited by*

*Peter Wellmann*

*Noboru Ohtani*

*Roland Rupp*

**WILEY-VCH**

# **Wide Bandgap Semiconductors for Power Electronics**

Materials, Devices, Applications

*Volume 2*

*Edited by*

*Peter Wellmann*

*Noboru Ohtani*

*Roland Rupp*

**WILEY-VCH**

## Editors

### **Prof. Peter Wellmann**

Friedrich-Alexander Universität  
Institut für Werkstoffwissenschaften  
Martensstraße 7  
91058 Erlangen  
Germany

### **Prof. Noboru Ohtani**

Kwansei Gakuin University  
School of Engineering  
2-1 Gakuen, Sanda  
669-1337 Hyogo  
Japan

### **Dr. Roland Rupp**

Infineon Technologies AG  
Am Campeon 1-15  
85579 Neubiberg  
Germany

**Cover Design:** Wiley

**Cover Image:** © Pictures by Infineon Technologies, all rights reserved.

All books published by **WILEY-VCH** are carefully produced. Nevertheless, authors, editors, and publisher do not warrant the information contained in these books, including this book, to be free of errors. Readers are advised to keep in mind that statements, data, illustrations, procedural details or other items may inadvertently be inaccurate.

**Library of Congress Card No.:**  
applied for

### **British Library Cataloguing-in-Publication Data**

A catalogue record for this book is available from the British Library.

### **Bibliographic information published by the Deutsche Nationalbibliothek**

The Deutsche Nationalbibliothek lists this publication in the Deutsche Nationalbibliografie; detailed bibliographic data are available on the Internet at <<http://dnb.d-nb.de>>.

© 2022 WILEY-VCH GmbH,  
Boschstr. 12, 69469 Weinheim,  
Germany

All rights reserved (including those of translation into other languages). No part of this book may be reproduced in any form – by photoprinting, microfilm, or any other means – nor transmitted or translated into a machine language without written permission from the publishers. Registered names, trademarks, etc. used in this book, even when not specifically marked as such, are not to be considered unprotected by law.

**Print ISBN:** 978-3-527-34671-4

**ePDF ISBN:** 978-3-527-82470-0

**ePub ISBN:** 978-3-527-82471-7

**oBook ISBN:** 978-3-527-82472-4

**Typesetting** Straive, Chennai, India  
**Printing and Binding**

Printed on acid-free paper

10 9 8 7 6 5 4 3 2 1

## Contents

### Volume 1

**Preface** *xiii*

### **Part I Silicon Carbide (SiC) 1**

- 1 Dislocation Formation During Physical Vapor Transport Growth of 4H-SiC Crystals 3**  
*Noboru Ohtani*
  - 1.1 Introduction 3
  - 1.2 Formation of Basal Plane Dislocations During PVT Growth of 4H-SiC Crystals 5
    - 1.2.1 Plan-View X-ray Topography Observations of Growth Front 5
    - 1.2.2 Cross-Sectional X-ray Topography Observations of Growth Front 9
    - 1.2.3 Characteristic BPD Distribution in PVT-Grown 4H-SiC Crystals 13
    - 1.2.4 BPD Multiplication During PVT Growth 15
  - 1.3 Dislocation Formation During Initial Stage of PVT Growth of 4H-SiC Crystals 18
    - 1.3.1 Preparation of 4H-SiC Wafers with Beveled Interface Between Grown Crystal and Seed Crystal 18
    - 1.3.2 Determination of Grown-Crystal/Seed Interface by Raman Microscopy 19
    - 1.3.3 X-ray Topography Observations of Dislocation Structure at Grown-Crystal/Seed Interface 22
    - 1.3.4 Formation Mechanism of BPD Networks and Their Migration into Seed Crystal 23
  - 1.4 Conclusions 28
  - References 30
- 2 Industrial Perspectives of SiC Bulk Growth 33**  
*Adrian R. Powell*
  - 2.1 Introduction 33

2.2	SiC Substrates for GaN LEDs	33
2.3	SiC Substrates for Power SiC Devices	34
2.4	SiC Substrates for High-Frequency Devices	35
2.5	Cost Considerations for Commercial Production of SiC	35
2.6	Raw Materials	36
2.7	Reactor Hot Zone	37
2.8	System Equipment	39
2.9	Yield	39
2.10	Turning Boules into Wafers	41
2.11	Crystal Grind	41
2.12	Wafer Slicing	42
2.13	Wafer Polish	44
2.14	Summary	44
	Acknowledgments	45
	References	45
<b>3</b>	<b>Homoepitaxial Growth of 4H-SiC on Vicinal Substrates</b>	<b>47</b>
	<i>Birgit Kallinger</i>	
3.1	Introduction	47
3.2	Fundamentals of 4H-SiC Homoepitaxy for Power Electronic Devices	47
3.2.1	4H-SiC Polytype Replication for Homoepitaxial Growth on Vicinal Substrates	48
3.2.2	Homoepitaxial Growth by Chemical Vapor Deposition (CVD) Process	52
3.2.3	Doping in Homoepitaxial Growth	53
3.3	Extended Defects in Homoepitaxial Layers	55
3.3.1	Classification of Extended Defects According to Glide Systems in 4H-SiC	56
3.3.2	Dislocation Reactions During Epitaxial Growth	57
3.3.3	Characterization Methods for Extended Defects in 4H-SiC Epilayers	59
3.4	Point Defects and Carrier Lifetime in Epilayers	62
3.4.1	Classification and General Properties of Point Defects in 4H-SiC	62
3.4.2	Basics on Recombination Carrier Lifetime in 4H-SiC	64
3.4.3	Carrier Lifetime-Affecting Point Defects	65
3.4.4	Carrier Lifetime Measurement in Epiwafers and Devices	68
3.5	Conclusion	69
	Acknowledgments	70
	References	70
<b>4</b>	<b>Industrial Perspective of SiC Epitaxy</b>	<b>75</b>
	<i>Albert A. Burk, Jr., Michael J. O'Loughlin, Denis Tsvetkov, and Scott Ustin</i>	
4.1	Introduction	75
4.2	Background	76
4.3	The Basics of SiC Epitaxy	76
4.4	SiC Epi Historical Origins	78
4.5	Planetary Multi-wafer Epitaxial Reactor Design Considerations	80

4.5.1	Rapidly Rotating Reactors	81
4.5.2	Horizontal Hot-Wall Reactors	82
4.6	Latest High-Throughput Epitaxial Reactor Status	82
4.7	Benefits and Challenges for Increasing Growth Rate in all Reactors	86
4.8	Increasing Wafer Diameters, Device Processing Considerations, and Projections	86
4.9	Summary	89
	Acknowledgment	90
	References	90
<b>5</b>	<b>Status of 3C-SiC Growth and Device Technology</b>	<b>93</b>
	<i>Peter Wellmann, Michael Schöler, Philipp Schuh, Mike Jennings, Fan Li, Roberta Nipoti, Andrea Severino, Ruggero Anzalone, Fabrizio Roccaforte, Massimo Zimbone, and Francesco La Via</i>	
5.1	Introduction, Motivation, Short Review on 3C-SiC	93
5.2	Nucleation and Epitaxial Growth of 3C-SC on Si	95
5.2.1	Growth Process	95
5.2.2	Defects	98
5.2.3	Stress	102
5.3	Bulk Growth of 3C-SiC	103
5.3.1	Sublimation Growth of (111)-oriented 3C-SiC on Hexagonal SiC Substrates	104
5.3.2	Sublimation Growth of 3C-SiC on 3C-SiC CVD Seeding Layers	105
5.3.3	Continuous Fast CVD Growth of 3C-SiC on 3C-SiC CVD Seeding Layers	110
5.4	Processing and Testing of 3C-SiC Based Power Electronic Devices	117
5.4.1	Prospects for 3C-SiC Power Electronic Devices	117
5.4.2	3C-SiC Device Processing	117
5.4.3	MOS Processing	118
5.4.4	3C-SiC/SiO <sub>2</sub> Interface Passivation	120
5.4.5	Surface Morphology Effects on 3C-SiC Thermal Oxidation	121
5.4.6	Thermal Oxidation Temperature Effects for 3C-SiC	122
5.4.7	Ohmic Contact Metalization	123
5.4.8	N-type 3C-SiC Ohmic Contacts	126
5.4.9	Ion Implantation	126
5.5	Summary	127
	Acknowledgements	127
	References	127
<b>6</b>	<b>Intrinsic and Extrinsic Electrically Active Point Defects in SiC</b>	<b>137</b>
	<i>Ulrike Grossner, Joachim K. Grillenberger, Judith Woerle, Marianne E. Bathan, and Johanna Müting</i>	
6.1	Characterization of Electrically Active Defects	141
6.1.1	Deep Level Transient Spectroscopy	141
6.1.1.1	Profile Measurements	143

6.1.1.2	Poole–Frenkel Effect	143
6.1.1.3	Laplace DLTS	143
6.1.2	Low-energy Muon Spin Rotation Spectroscopy	144
6.1.2.1	μSR and Semiconductors	144
6.1.3	Density Functional Theory	145
6.2	Intrinsic Electrically Active Defects in SiC	146
6.2.1	The Carbon Vacancy, $V_C$	147
6.2.2	The Silicon Vacancy, $V_{Si}$	152
6.3	Transition Metal and Other Impurity Levels in SiC	153
6.4	Summary	159
	References	163
<b>7</b>	<b>Dislocations in 4H-SiC Substrates and Epilayers</b>	<b>169</b>
	<i>Balaji Raghathamachar and Michael Dudley</i>	
7.1	Introduction	169
7.2	Dislocations in Bulk 4H-SiC	170
7.2.1	Micropipes (MPs) and Closed-core Threading Screw Dislocations (TSDs)	170
7.2.2	Basal Plane Dislocations (BPDs)	171
7.2.3	Threading Edge Dislocations (TEDs)	171
7.2.4	Interaction between BPDs and TEDs	171
7.2.4.1	Hopping Frank–Read Source of BPDs	171
7.2.5	Threading Mixed Dislocations (TMDs) in 4H-SiC	173
7.2.5.1	Reaction Between Threading Dislocations with Burgers Vectors of $-c + a$ and $c + a$ Wherein the Opposite $c$ -Components Annihilate Leaving Behind the Two $a$ -Components	174
7.2.5.2	Reaction Between Threading Dislocations with Burgers Vectors of $-c$ and $c + a$ Leaving Behind the $a$ -Component	175
7.2.5.3	Reaction Between Opposite-sign Threading Screw Dislocations with Burgers Vectors $c$ and $-c$	175
7.2.5.4	Nucleation of Opposite Pair of $c + a$ Dislocations and Their Deflection	175
7.2.5.5	Deflection of Threading $c + a$ , $c$ and Creation of Stacking Faults	177
7.2.6	Prismatic Slip during PVT growth 4H-SiC Boules	180
7.2.7	Relationship Between Local Basal Plane Bending and Basal Plane Dislocations in PVT-grown 4H-SiC Substrate Wafers	181
7.2.8	Investigation of Dislocation Behavior at the Early Stage of PVT-grown 4H-SiC Crystals	181
7.3	Dislocations in Homoepitaxial 4H-SiC	184
7.3.1	Conversion of BPDs into TEDs	184
7.3.2	Susceptibility of Basal Plane Dislocations to the Recombination-Enhanced Dislocation Glide in 4H Silicon Carbide	184
7.3.3	Nucleation of TEDs, BPDs, and TSDs at Substrate Surface Damage	188
7.3.4	Nucleation Mechanism of Dislocation Half-Loop Arrays in 4H-SiC Homo-Epitaxial Layers	191

7.3.5	V- and Y-shaped Frank-type Stacking Faults	192
7.4	Summary	192
	Acknowledgments	195
	References	195
<b>8</b>	<b>Novel Theoretical Approaches for Understanding and Predicting Dislocation Evolution and Propagation</b>	<b>199</b>
	<i>Binh Duong Nguyen and Stefan Sandfeld</i>	
8.1	Introduction	199
8.2	General Modeling and Simulation Approaches	200
8.3	Continuum Dislocation Modeling Approaches	201
8.3.1	Alexander–Haasen Model	201
8.3.2	Continuum Dislocation Dynamics Models	202
8.3.2.1	The Simplest Model: Straight Parallel Dislocation with the Same Line Direction	203
8.3.2.2	The “Groma” Model: Straight Parallel Dislocations with Two Line Directions	203
8.3.2.3	The Kröner–Nye Model for Geometrically Necessary Dislocations	204
8.3.2.4	Three-dimensional Continuum Dislocation Dynamics (CDD)	204
8.4	Example 1: Comparison of the Alexander–Haasen and the Groma Model	206
8.4.1	Governing Equations	206
8.4.2	Physical System and Model Setup	206
8.4.3	Results and Discussion	209
8.5	Example 2: Dislocation Flow Between Veins	211
8.5.1	A Brief Introduction to Dislocation Patterning and the Similitude Principle	211
8.5.2	Physical System and Model Setup	213
8.5.3	Geometry and Initial Values	214
8.5.4	Results and Discussion	215
8.6	Summary and Conclusion	219
	References	220
<b>9</b>	<b>Gate Dielectrics for 4H-SiC Power Switches: Understanding the Structure and Effects of Electrically Active Point Defects at the 4H-SiC/SiO<sub>2</sub> Interface</b>	<b>225</b>
	<i>Gregor Pobegen and Thomas Aichinger</i>	
9.1	Introduction	225
9.2	Electrical Impact of Traps on MOSFET Characteristics	225
9.2.1	Sub threshold Sweep Hysteresis	226
9.2.2	Preconditioning Measurement	231
9.2.3	Bias Temperature Instability	233
9.2.4	Reduced Channel Electron Mobility	235
9.3	Microscopic Nature of Electrically Active Traps Near the Interface	237
9.3.1	The P <sub>bc</sub> Defect and the Subthreshold Sweep Hysteresis	237

9.3.2	The Intrinsic Electron Trap and the Reduced MOSFET Mobility	238
9.3.3	Point Defect Candidates for BTI	240
9.4	Conclusions and Outlook	242
	References	243

## **10 Epitaxial Graphene on Silicon Carbide as a Tailorable Metal–Semiconductor Interface** 249

*Michael Krieger and Heiko B. Weber*

10.1	Introduction	249
10.2	Epitaxial Graphene as a Metal	249
10.3	Fabrication and Structuring of Epitaxial Graphene	250
10.3.1	Epitaxial Growth by Thermal Decomposition	250
10.3.2	Intercalation	251
10.3.3	Structuring of Epitaxial Graphene Layers and Partial Intercalation	252
10.4	Epitaxial Graphene as Tailorable Metal/Semiconductor Contact	253
10.4.1	Ohmic Contacts	254
10.4.2	Schottky Contacts	256
10.5	Monolithic Epitaxial Graphene Electronic Devices and Circuits	257
10.5.1	Discrete Epitaxial Graphene Devices	257
10.5.2	Monolithic Integrated Circuits	259
10.6	Novel Experiments on Light–Matter Interaction Enabled by Epitaxial Graphene	260
10.6.1	High-Frequency Operation and Ultimate Speed Limits of Schottky Diodes	260
10.6.2	Transparent Electrical Access to SiC for Novel Quantum Technology Applications	263
10.7	Conclusion	264
	Acknowledgments	265
	References	265

## **11 Device Processing Chain and Processing SiC in a Foundry Environment** 271

*Arash Salemi, Minseok Kang, Woongje Sung, and Anant K. Agarwal*

11.1	Introduction	271
11.2	DMOSFET Structure	271
11.3	Process Integration of SiC MOSFETs	273
11.3.1	Lithography	283
11.3.2	SiC Etching	283
11.3.3	Ion Implantation and Activation Annealing	290
11.3.4	Oxidation and Oxide	293
11.3.5	Post Oxidation Annealing	296
11.3.6	Poly-Si Deposition	298
11.3.7	Backside Thinning and Waffle Substrates	300
11.3.8	Ohmic Contacts and Metallization	301
11.3.9	Polyimide Deposition	302

- 11.4 Commercial Foundries for Si and SiC Devices 303
  - 11.4.1 Cost Model 303
    - 11.4.1.1 Cost Roadmap for WBG Devices 303
  - 11.4.2 New Equipment and Processing Requirements 305
- 11.5 Dedicated Foundries vs. Commercial Foundries 306
  - References 307

## **12 Unipolar Device in SiC: Diodes and MOSFETs 319**

*Sei-Hyung Ryu*

- 12.1 Introduction 319
- 12.2 Unipolar Diodes – 4H-SiC JBS Diodes 320
  - 12.2.1 Optimization of 4H-SiC JBS Diodes 323
    - 12.2.1.1 Injection from the p<sup>+</sup> Regions for Surge Operation 324
    - 12.2.1.2 Trench JBS Diodes 326
    - 12.2.1.3 Use of Low Work Function Metal for Anode Metal 327
- 12.3 Unipolar Switches: Power MOSFETs 329
  - 12.3.1 4H-SiC Power MOSFET Structures 332
    - 12.3.1.1 DMOSFETs 332
    - 12.3.1.2 Trench MOSFETs 337
  - 12.3.2 Advanced Power MOSFET Structures in 4H-SiC 342
    - 12.3.2.1 Superjunction MOSFETs in 4H-SiC 342
    - 12.3.2.2 Integrated JBS Diodes in 4H-SiC Power MOSFETs 345
- 12.4 Summary 346
  - References 348

## **Volume 2**

### **13 Ultra-High-Voltage SiC Power Device 353**

*Yoshiyuki Yonezawa and Koji Nakayama*

### **14 SiC Reliability Aspects 387**

*Josef Lutz and Thomas Basler*

### **15 Industrial Systems Using SiC Power Devices 433**

*Nando Kaminski*

### **16 Special Focus on HEV and EV Applications: Activities of Automotive Industries Applying SiC Devices for Automotive Applications 467**

*Kimimori Hamada, Keiji Toda, Hiromichi Nakamura, Shigeharu Yamagami, and Kazuhiro Tsuruta*

### **17 Point Defects in Silicon Carbide for Quantum Technology 503**

*András Csóré and Adam Gali*

**Part II Gallium Nitride (GaN), Diamond, and Ga<sub>2</sub>O<sub>3</sub> 529**

- 18 Ammonothermal and HVPE Bulk Growth of GaN 531**  
*Robert Kucharski, Tomasz Sochacki, Boleslaw Lucznik, Mikolaj Amilusik, Karolina Grabianska, Malgorzata Iwinska, and Michal Bockowski*
- 19 GaN on Si: Epitaxy and Devices 555**  
*Hidekazu Umeda*
- 20 Growth of Single Crystal Diamond Wafers for Future Device Applications 583**  
*Matthias Schreck*
- 21 Diamond Wafer Technology, Epitaxial Growth, and Device Processing 633**  
*Hideaki Yamada, Hiromitsu Kato, Shinya Ohmagari, and Hitoshi Umezawa*
- 22 Gallium Oxide: Material Properties and Devices 659**  
*Masataka Higashiwaki*
- Index 681**

## Contents

### Volume 1

Preface *xiii*

### Part I Silicon Carbide (SiC) 1

- 1 Dislocation Formation During Physical Vapor Transport Growth of 4H-SiC Crystals 3**  
*Noboru Ohtani*
- 2 Industrial Perspectives of SiC Bulk Growth 33**  
*Adrian R. Powell*
- 3 Homoepitaxial Growth of 4H-SiC on Vicinal Substrates 47**  
*Birgit Kallinger*
- 4 Industrial Perspective of SiC Epitaxy 75**  
*Albert A. Burk, Jr., Michael J. O'Loughlin, Denis Tsvetkov, and Scott Ustin*
- 5 Status of 3C-SiC Growth and Device Technology 93**  
*Peter Wellmann, Michael Schöler, Philipp Schuh, Mike Jennings, Fan Li, Roberta Nipoti, Andrea Severino, Ruggero Anzalone, Fabrizio Roccaforte, Massimo Zimbone, and Francesco La Via*
- 6 Intrinsic and Extrinsic Electrically Active Point Defects in SiC 137**  
*Ulrike Grossner, Joachim K. Grillenberger, Judith Woerle, Marianne E. Bathen, and Johanna Müting*

- 7 Dislocations in 4H-SiC Substrates and Epilayers 169**  
*Balaji Raghothamachar and Michael Dudley*
- 8 Novel Theoretical Approaches for Understanding and Predicting Dislocation Evolution and Propagation 199**  
*Binh Duong Nguyen and Stefan Sandfeld*
- 9 Gate Dielectrics for 4H-SiC Power Switches: Understanding the Structure and Effects of Electrically Active Point Defects at the 4H-SiC/SiO<sub>2</sub> Interface 225**  
*Gregor Pobegen and Thomas Aichinger*
- 10 Epitaxial Graphene on Silicon Carbide as a Tailorable Metal–Semiconductor Interface 249**  
*Michael Krieger and Heiko B. Weber*
- 11 Device Processing Chain and Processing SiC in a Foundry Environment 271**  
*Arash Salemi, Minseok Kang, Woongje Sung, and Anant K. Agarwal*
- 12 Unipolar Device in SiC: Diodes and MOSFETs 319**  
*Sei-Hyung Ryu*
- Volume 2**
- 13 Ultra-High-Voltage SiC Power Device 353**  
*Yoshiyuki Yonezawa and Koji Nakayama*
- 13.1 Introduction 353
- 13.2 Ultra-high-voltage SiC PiN diode and SiC-IGBT 355
- 13.3 Reverse Characteristics of SiC Bipolar Device 356
- 13.3.1 Relationship Between Thickness and Density of Drift Layer and Breakdown Voltage 356
- 13.3.2 Termination Structure of SiC Bipolar Devices 357
- 13.4 Carrier Lifetime Dependence on the Characteristics of Bipolar Device 358
- 13.4.1 Forward Characteristics of pn Diode 360
- 13.4.1.1 Analysis of Characteristics Under Low-Level Injection 360
- 13.4.1.2 Analysis of Carriers in the Drift Layer Under High-Level Injection 362
- 13.4.1.3 Relationship Between Carrier Life, Drift Layer Thickness, and Drift Layer Voltage Drop 363
- 13.4.2 Reverse Characteristics of pn Diode 365

13.4.2.1	Reverse Leakage Current Characteristics	365
13.4.3	Dynamic Characteristics of pn Diode	365
13.4.3.1	Reverse and Forward Recovery of Characteristics	365
13.4.3.2	Open-Circuit Voltage Decay	366
13.4.3.3	Comparison of Reverse and Forward Recovery Characteristics and OCVD	368
13.5	Design and Device Performance of Bipolar Device	370
13.5.1	Carrier lifetime dependence	371
13.5.2	Loss Estimation of Bipolar Device	373
13.6	Current Status of SiC Bipolar Device	377
13.6.1	Device Performance of 16 kV Class SiC-IGBT	378
13.6.2	Device Characteristics of higher-than-20 kV Class SiC-IGBT	382
13.6.3	Other Bipolar Devices Issues	383
	References	384
<b>14</b>	<b>SiC Reliability Aspects</b>	<b>387</b>
	<i>Josef Lutz and Thomas Basler</i>	
14.1	Ruggedness and Overload Events	387
14.1.1	Short-circuit Ruggedness of SiC MOSFETs	387
14.1.2	Surge-current Ruggedness	394
14.1.3	Avalanche Capability	403
14.2	Cosmic-Ray Stability	412
14.3	Thermomechanical Reliability	414
14.3.1	Temperature-sensitive Electrical Parameters	416
14.3.2	Execution of Power-cycling Tests	419
14.3.3	Evaluation of SiC Power-cycling Tests	421
14.4	New Power-module Technologies with Sufficient Reliability	422
14.4.1	Improved Die-attach Technologies	422
14.4.2	Improved Top-Side Interconnections	424
	Acknowledgments	426
	References	426
<b>15</b>	<b>Industrial Systems Using SiC Power Devices</b>	<b>433</b>
	<i>Nando Kaminski</i>	
15.1	Introduction	433
15.1.1	Benefits of SiC Devices	433
15.1.2	Competition by Other Technologies	436
15.2	DC/DC Converters	437
15.3	Solid-State Transformer (SST)	443
15.3.1	Traction	443
15.3.2	Power Grid	444
15.4	Wireless Charging	445

15.5	Inductive Heating	446
15.5.1	Domestic Systems	446
15.5.2	Industrial Systems	446
15.6	Photovoltaic	447
15.6.1	Residential Systems	447
15.6.2	Commercial, Industrial, and Utility Size Systems	449
15.7	DC Grids	451
15.7.1	Low- and Medium-Voltage DC Grids	451
15.7.2	DC Breakers	452
15.8	High-Voltage DC (HVDC)	452
15.8.1	HVDC Transmission	452
15.8.2	HVDC Breakers	454
15.9	Drives	455
15.9.1	Industrial Drives	455
15.9.2	Wind Energy	457
15.9.3	Traction	458
15.10	Conclusions	459
	Acknowledgements	460
	References	460
<b>16</b>	<b>Special Focus on HEV and EV Applications: Activities of Automotive Industries Applying SiC Devices for Automotive Applications</b>	<b>467</b>
	<i>Kimimori Hamada, Keiji Toda, Hiromichi Nakamura, Shigeharu Yamagami, and Kazuhiro Tsuruta</i>	
16.1	Background (PDPlus LLC)	467
16.2	The Challenge of SiC Power Devices Introductions on Prototype HEVs and FCVs (TOYOTA MOTOR CORPORATION)	469
16.2.1	Progress of Electrification	469
16.2.2	Demonstration of Electrified Vehicles	470
16.3	Introduction of Boost Converter Using SiC Semiconductor for New FCV Drive (HONDA MOTOR CO., LTD.)	472
16.3.1	Introduction	472
16.3.2	Configuration of the Electric Power Plant System for New FCV	472
16.3.3	FCVCU	473
16.3.3.1	Circuit Configuration	473
16.3.3.2	Full SiC-IPM	473
16.3.3.3	Magnetic Coupling and Interleave Operation	474
16.3.3.4	Control Methods	475
16.3.3.5	Effects on Smaller Size and Higher Efficiency	477
16.3.3.6	Quietness	478
16.3.3.7	Noise Countermeasures	478

16.3.3.8	Structure of the FCVCU	479
16.3.4	Conclusions	480
16.4	Development of Module Technologies to Bring Out SiC Power Device Performances (TOYOTA MOTOR CORPORATION)	481
16.4.1	Power Card Structure for Double-Side Cooling Technology	481
16.4.2	New Transient Liquid Phase Structure for High-Temperature Applications	481
16.4.3	Ni Micro-Plating Bonding	483
16.5	SiC-MOSFET Switching Characteristics and Gate Driver Circuits for Automotive Application (NISSAN MOTOR CO., LTD.)	485
16.5.1	Introduction	485
16.5.2	Basics of Switching Characteristics	485
16.5.3	Various Gate Driver Circuits	487
16.5.4	Conclusion	489
16.6	R&D of SiC Power Devices for Automotive Applications (DENSO CORPORATION)	489
16.6.1	Introduction	489
16.6.2	Ultra-Low-Loss SiC-MOSFET for Cost Reduction	491
16.6.3	Proposed 4H-SiC Trench MOSFET Structure	491
16.6.4	Characteristics of the Developed MOSFET	494
16.6.4.1	Static Characteristics of the Optimized Structure	494
16.6.4.2	Dynamic Behavior of the Optimized Structure	495
16.6.5	Measurements of Reliability	497
16.6.6	Suppression of Bipolar Degradation in the Presented MOSFETs [30]	497
16.6.7	Summary	500
	Acknowledgments	500
	References	501
<b>17</b>	<b>Point Defects in Silicon Carbide for Quantum Technology</b>	<b>503</b>
	<i>András Csóré and Adam Gali</i>	
17.1	Introduction	503
17.2	Silicon Carbide: Polytypes and Types of Relevant Point Defects	504
17.3	Point Defect Single Photon Sources and Quantum Bits	507
17.3.1	Divacancy	508
17.3.2	Si-vacancy	510
17.3.3	Carbon Antisite-Vacancy Pair	513
17.3.4	Nitrogen-Vacancy Pair	514
17.3.5	Other Defects	515
17.4	Conclusion	517
	Acknowledgments	518
	References	518

**Part II Gallium Nitride (GaN), Diamond, and Ga<sub>2</sub>O<sub>3</sub> 529**

- 18 Ammonothermal and HVPE Bulk Growth of GaN 531**  
*Robert Kucharski, Tomasz Sochacki, Boleslaw Lucznik, Mikolaj Amilusik, Karolina Grabianska, Malgorzata Iwinska, and Michal Bockowski*
- 18.1 Introduction 531
  - 18.2 HVPE Method – History and State of the Art 533
  - 18.3 Ammonothermal Method – History and State of the Art 536
  - 18.4 HVPE-GaN-on-Ammono-GaN – State of the Art 542
    - 18.4.1 Bulk Growth – Challenges 543
    - 18.4.2 Doping 546
      - 18.4.2.1 Doping with Donors 546
      - 18.4.2.2 Doping with Acceptors 549
  - 18.5 Summary 550
    - Acknowledgments 551
    - References 551
- 19 GaN on Si: Epitaxy and Devices 555**  
*Hidekazu Umeda*
- 19.1 Introduction 555
  - 19.2 GaN Epitaxy on Si Substrate 556
    - 19.2.1 GaN Epitaxial Method and Doping 556
      - 19.2.1.1 Metal–Organic Chemical Vapor Deposition (MOCVD) 556
      - 19.2.1.2 N, P-Type Doping 556
      - 19.2.1.3 Doping for Semi-insulation Layer 557
    - 19.2.2 Substrates for GaN Epitaxy 557
      - 19.2.2.1 GaN 557
      - 19.2.2.2 Sapphire 558
      - 19.2.2.3 SiC 558
      - 19.2.2.4 Si 559
    - 19.2.3 Epitaxial Growth Technology on Si Substrate 559
      - 19.2.3.1 Crystal Orientation of Si Substrate 559
      - 19.2.3.2 Nucleation Layer 559
      - 19.2.3.3 Buffer Layer 560
      - 19.2.3.4 AlGa<sub>N</sub>/GaN Active Layer with Polarization Effect 561
  - 19.3 Lateral GaN Devices on Si Substrate 564
    - 19.3.1 Device Structure and Fabrication Process 564
    - 19.3.2 Structures for E-Mode Operation 566
    - 19.3.3 E-Mode GaN Gate-Injection Transistor (GIT) on Si Substrate 567
      - 19.3.3.1 Device Structure and Operational Principle 567
      - 19.3.3.2 DC Performance of GIT 568
      - 19.3.3.3 Switching Performance of GIT 570

19.4	Application of GaN HFET	571
19.5	Integration of Lateral GaN Devices	573
19.6	Summary	576
	Acknowledgments	577
	References	577
<b>20</b>	<b>Growth of Single Crystal Diamond Wafers for Future Device Applications</b>	<b>583</b>
	<i>Matthias Schreck</i>	
20.1	Introduction	583
20.2	High-Pressure High-Temperature (HPHT) Synthesis	584
20.2.1	Basic Concepts and Technical Realizations	584
20.2.2	The Temperature Gradient Method	586
20.2.3	Chemical Purity and Classification	587
20.2.4	Morphology and Structural Quality	588
20.2.5	State of the Art in Crystal Size	589
20.2.6	Boron Doping	590
20.3	Chemical Vapor Deposition (CVD)	591
20.3.1	Basic Principles	591
20.3.1.1	The Mechanism of Diamond Growth by CVD	591
20.3.1.2	Gas Mixtures for Diamond CVD	593
20.3.1.3	The Role of Trace Gases	594
20.3.1.4	Experimental Setups	595
20.3.1.5	Growth Rate and Gas Temperature	598
20.3.1.6	Nucleation by Seeding	599
20.3.1.7	Bias-Enhanced Nucleation (BEN)	599
20.3.2	Examples of Polycrystalline CVD Diamond Layers	601
20.3.3	CVD Growth of Single Crystals	602
20.3.4	Homoepitaxy	603
20.3.4.1	Homoepitaxial Growth on Different Crystals Faces	603
20.3.4.2	Single Crystal Seed Recovery	604
20.3.4.3	Size Increase and Mosaic Growth	605
20.3.5	Heteroepitaxy	605
20.3.5.1	Growth Substrates for Heteroepitaxy	605
20.3.5.2	Bias-Enhanced Nucleation on Iridium: Phenomenology and Mechanism	607
20.3.5.3	Structural Improvement with Film Thickness	609
20.3.5.4	Multilayer Substrates for Scaling to Wafer Size	611
20.3.5.5	The State of the Art in Scaling and Mosaic Spread	613
20.3.5.6	Intrinsic Stress and Its Correlation with Dislocations	614
20.3.5.7	Heteroepitaxy on (111)-Oriented Substrates	614
20.3.5.8	The Microneedle Approach	615

- 20.3.6 Advanced Concepts for Structural Improvement 617
- 20.3.6.1 Epitaxial Lateral Overgrowth 617
- 20.3.6.2 Dislocation Stopping by W or Ta Atoms 618
- 20.4 State of the Art and Outlook 619
- Acknowledgments 619
- References 619

## **21 Diamond Wafer Technology, Epitaxial Growth, and Device Processing 633**

*Hideaki Yamada, Hiromitsu Kato, Shinya Ohmagari, and Hitoshi Umezawa*

- 21.1 Diamond Epitaxial Growth and Wafers 633
- 21.2 n-Type Doping and Processing 638
- 21.3 p-Type Doping and Processing 642
- 21.4 Devices 645
- References 650

## **22 Gallium Oxide: Material Properties and Devices 659**

*Masataka Higashiwaki*

- 22.1 Introduction 659
- 22.2 Physical Properties of  $\text{Ga}_2\text{O}_3$  660
  - 22.2.1 Polymorphs 660
  - 22.2.2 Material Properties of  $\beta\text{-Ga}_2\text{O}_3$  660
- 22.3 Melt Bulk Growth 662
- 22.4 Epitaxial Growth 662
  - 22.4.1 MBE 663
  - 22.4.2 HVPE 664
  - 22.4.3 MOCVD 664
  - 22.4.4 Mist CVD 665
- 22.5 Vertical Diodes 665
  - 22.5.1 SBD with HVPE-Grown Drift Layer 665
  - 22.5.2 Field-Plated SBD 666
  - 22.5.3 Field-Plated SBD with Guard Ring Formed by Nitrogen-Ion Implantation 666
  - 22.5.4 Trench SBD 667
  - 22.5.5  $\alpha\text{-Ga}_2\text{O}_3$  SBD 667
  - 22.5.6 Heterojunction p-Amorphous Oxide/n- $\text{Ga}_2\text{O}_3$  Diode 668
- 22.6 Lateral FETs 668
  - 22.6.1 MESFET 668
  - 22.6.2 Depletion-Mode MOSFET 669
  - 22.6.3 Field-Plated MOSFET 671
  - 22.6.4 Modulation-Doped FET 671
  - 22.6.5 Normally Off FET 672

- 22.7 Vertical FETs 672
  - 22.7.1 Current Aperture FET 673
  - 22.7.2 Fin Channel FET 673
- 22.8 Summary 674
  - References 674
  
- Index 681**



## Preface

### Introduction

The scope of this edited book is to provide a state of the art of the technology and application of SiC and related wide bandgap materials. The focus lies on the material SiC with 16 review articles from internationally well-known experts covering major aspects of fundamental physics, applied science, as well as industrial development and manufacturing. In addition, five experts are reporting on the technological status of further wide bandgap materials GaN, diamond, and Ga<sub>2</sub>O<sub>3</sub>, which have the potential to even outperform SiC with respect to certain physical properties relevant for power electronics.

The semiconductor Si has dominated the fabrication of electronic devices for switching of electrical currents or for the application in microelectronics almost since the beginning of semiconductor technology in the early 1950s. For the application in power electronic devices, however, two major material properties limit the performance of Si: the medium breakdown field limits the achievable conductivity at a certain desired breakdown voltage as well as the medium heat conductivity hinders the release of excess power during device operation (e.g. overcurrent, short circuit, avalanche) and, hence, may cause thermal failure. From a physical point of view, wide bandgap materials like SiC, Diamond, GaN, AlN, and Ga<sub>2</sub>O<sub>3</sub> exhibit a much higher breakdown field that outperform their medium bandgap counterparts like Si and GaAs by a factor of 10 and more (see Table 1). Due to their strong covalent chemical bonding, the wide bandgap semiconductors diamond and SiC show a significant higher heat conductivity than the standard semiconductor Si. Hence, SiC- and diamond-based power electronic devices can handle much higher power densities than Si devices would do.

A key parameter for the choice of the proper semiconductor in power electronics is the so-called on-resistance of a power semiconductor device (Figure 1). Related to this, the Baliga's figure of merit (BFOM) defined as  $\epsilon\mu E_C^3$  ( $\epsilon$  = dielectric strength,  $\mu$  = charge carrier mobility,  $E_C$  = breakdown field) provides a selection rule for the proper choice of a semiconductor material for power electronic transistors. In literature, BFOM values are often calculated from idealized material properties that do not reflect the conditions under real device operation. Nevertheless, the BFOM value allows to rate the ultimate potential of each semiconductor related

**Table 1** Physical properties (room temperature values) of wide bandgap semiconductors for power electronic applications in comparison to classic semiconductor materials (data from [1–3]).

	4H-SiC	GaN	AlN	$\beta$ -Ga <sub>2</sub> O <sub>3</sub>	C	Si
Lattice parameter (Å)	$a = 3.08$ Hexagonal	$a = 3.19$ Hexagonal	$a = 3.11$ Hexagonal	$a = 12.23$ $b = 3.04$ $c = 5.80$ $\beta = 103.7^\circ$ Monoclinic	3.57 Cubic	5.43 Cubic
$E_G$ (eV)	3.2	3.44	6.2	4.8	5.5	1.1
$E_B$ (10 <sup>5</sup> V/cm)	40	50	150	80	100	3
$\epsilon$	9.7	10.4	9.1	10	5.7	11.9
$\lambda$ (W/cm/K)	3–5	1.3	2.9	0.23	20	1.5
$v_S$ (10 <sup>7</sup> cm/s)	2.5	2.5	2.5 <sup>approx.</sup>	2	2.7	1
$\mu_n$ (cm <sup>2</sup> /V/s)	<900	<1000	300	250	<2200	1400
$E_D$ (meV)	60 (N)	22 (Si)	90–250 (Si)	20–30 (Sn)		45 (P)
$E_A$ (meV)	250 (Al)	160 (Mg)	500 (Mg)		400 (B)	44 (B)
$T_S$ (°C)	2830	2500	3000	1740	3900	1420
Doping capability	n-type <sup>med</sup> p-type <sup>high</sup>	n-type <sup>med</sup> p-type <sup>high</sup>	n-type <sup>high</sup> p-type difficult	n-type <sup>med</sup> No p-type	n-type difficult p-type <sup>high</sup>	n-type p-type
Baliga FOM $\epsilon\mu E_B^3$ with relation to Si	500	1100	8100	1350	11,000	1
Johnson FOM $v_S E_B / 2\pi$ with relation to Si	25	31	75	40	68	1
Native wafer material size	150 mm 200 mm <sup>dem</sup>	50 mm <sup>lowav</sup> 100 mm <sup>lowav</sup>	50 mm <sup>dem</sup>	150 mm <sup>dem</sup>	c. 100 mm <sup>dem,lim</sup>	200 mm 300 mm 450 mm <sup>dev</sup>
Maturity of technology	c)	Power <sup>b)</sup> High frequency <sup>c)</sup> Optoelectronics <sup>d)</sup>	a)	a),b)	a)	d)

approx., approximated value; med, medium excitation energy; high, high excitation energy; dev, developed; dem, demonstrated; lim, limited crystal quality; lowav, low availability

The calculated Baliga FOM is based on idealized charge carrier transport properties that are usually not realized in a real electronic device. The usage of the materials breakdown field  $E_B$  as critical breakdown field  $E_C$  is an overestimation. Also, in the case of the Johnson FOM, the critical electrical field  $E_C$  was approximated by the breakdown field  $E_B$ , which is the upper limit.

- a) R&D.
- b) Demonstrators.
- c) Well developed.
- d) Mature.

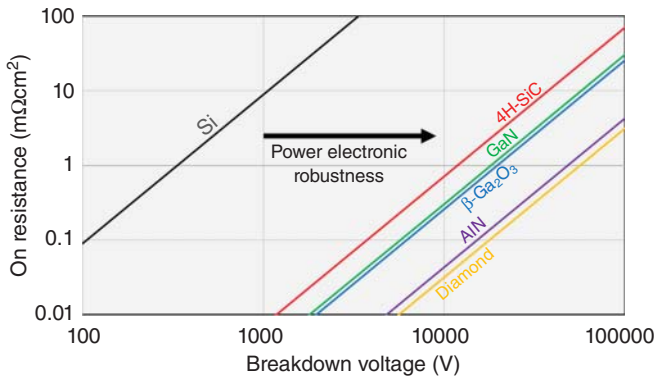


**Figure 1** Relation of the on-resistance and the breakdown voltage of a power semiconductor device. The underlying material properties have been listed in Table 1. In general, a larger bandgap causes a significant reduction of the on-resistance at a given device operation voltage.

to power electronics. In addition to the BFOM value, a large heat conductivity of the semiconductor material is quite favorable in power electronics. Among the wide bandgap semiconductors listed in Figure 1 and Table 1, SiC outperforms its counterpart by simultaneously exhibiting a large BFOM value (compared to Si), a great heat conductivity (compared to GaN and  $\text{Ga}_2\text{O}_3$ ), and a quite mature device-processing technology that makes use of major parts of Si processing lines. In addition, high-quality SiC wafer substrates are available with a diameter of 150 mm, and even the 200 mm size has been demonstrated. Further, a quite significant cost down for the SiC substrate costs (US\$/mm<sup>2</sup>) in the range of 10%/a–12%/a has been observed in the last two decades since the introduction of the very first SiC diode to the market in year 2001.

Another important issue for the application of a wide bandgap material in an electronic device is the capability to carry out intentional doping by donor and acceptor atoms to tailor electron and hole transport and to establish bipolar device operation. From the application point of view, at least one kind of doping, i.e. by donor or acceptor atoms, is necessary to establish unipolar device operation. In this context, SiC exhibits reasonable n-type and p-type doping options using the donor nitrogen and the acceptors boron and aluminum, respectively.

Wide bandgap semiconductors also exhibit superior physical properties for the application in high-frequency switching devices. In this context, the Johnson figure of merit  $v_s E_C / 2\pi$  ( $v_s$  = charge carrier saturation velocity,  $E_C$  = critical electrical field in the device structure) may be applied for materials selection (Table 1). From the application point of view, GaN epitaxial layers grown on semi-insulating SiC substrates are widely used for the fabrication of high-frequency and medium-power switches, as they are needed in mobile communication networks. This kind of application of SiC profits from the progress in bulk growth of conductive n-type conducting 4H-SiC substrates.

To link the high potential of the wide bandgap semiconductor SiC with the technologic implementation capabilities, all chapters on defects, bulk growth, epitaxial growth, and device processing stemming from fundamental physics and/or materials science and engineering are combined with chapters that comprise the status of the industrial-driven technology development. Following this structure in Part I of the book, the reader gains a comprehensive insight into today's SiC technology. The strong focus on the semiconductor SiC is related to the fact that the well-developed technology is ready to replace the standard semiconductor Si in power electronics. To point out that the materials focus on SiC is not dogmatic, also related wide bandgap materials featuring extraordinary power electronic-related properties, i.e. GaN, diamond, and Ga<sub>2</sub>O<sub>3</sub>, are surveyed in the shorter Part II of the book.

September 2021

*Peter Wellmann*, Erlangen  
*Noboru Ohtani*, Sanda  
*Roland Rupp*, Lauf a. d. Pegnitz

## References

- 1 Madelung, O. (ed.) (1996). *Semiconductors – Basic Data*, Data in Science and Technology, 2e, vol. 1. Berlin, Heidelberg, New York: Springer.
- 2 Levinshtein, M.E., S.L. Rumyantsev, and M.S. Shur. *Properties of advanced semiconductor materials: GaN, AlN, InN, BN, SiC, SiGe*. 2001.
- 3 Mastro, M.A., Kuramata, A., Calkins, J. et al. (2017). *Opportunities and future directions for Ga<sub>2</sub>O<sub>3</sub>*. *ECS J. Solid State Sci. Technol.* 6 (5): 356–359.

## **Part I**

### **Silicon Carbide (SiC)**



# 1

## Dislocation Formation During Physical Vapor Transport Growth of 4H-SiC Crystals

*Noboru Ohtani*

*Kwansei Gakuin University, School of Engineering, 2-1 Gakuen, Sanda, Hyogo 669-1337, Japan*

### 1.1 Introduction

Silicon carbide (SiC) is the leading candidate among wide-bandgap semiconductor materials for next-generation power semiconductor devices. Over recent decades, the quality of SiC single crystals has improved considerably, thereby making it feasible to fabricate high-performance SiC power devices. 4H-SiC epitaxial wafers of 100 and 150 mm in diameter, with low dislocation density are already available in the market and have been used to fabricate high-performance SiC power devices [1]. However, the widespread commercialization of such devices remains hindered by technological issues related to SiC crystal growth. It is abundantly clear that further successful development of SiC semiconductor technology relies on understanding the process of SiC crystal growth and thus improving the technology for manufacturing large high-quality SiC crystals.

In this chapter, I describe recent progress in understanding the formation of defects during physical vapor transport (PVT) growth of SiC, focusing particularly on the formation of dislocations in 4H-SiC. Currently, commercially available SiC bulk crystals are almost always grown by PVT, namely, by the modified Lely method [2]. However, dislocation formation during the PVT growth of bulk SiC crystals remains a major obstacle to realizing high-performance SiC power devices. Certain types of dislocation are detrimental to the yield and reliability of SiC power devices. Dislocations in PVT-grown SiC crystals are classified broadly into two types, namely, (i) threading dislocations extending along the *c*-axis and (ii) basal plane dislocations (BPDs) lying in the basal plane. Threading dislocations, particularly threading screw dislocations (TSDs), degrade the blocking capabilities of SiC diodes [3–5], whereas BPDs have a serious impact on the reliability of unipolar devices such as SiC metal oxide semiconductor field-effect transistors (MOSFETs) and junction gate field-effect transistors (JFETs) [6, 7] as well as SiC bipolar devices [8, 9]. Therefore, over the decades, considerable effort has gone into reducing the TSD and BPD densities in SiC crystals.

TSDs and BPDs differ markedly in how they form during the PVT growth of SiC crystals. Most TSDs are inherited from the seed crystal and often form in the initial

stage of crystal growth [10–12]. BPDs can also be inherited from the seed crystal and form during the initial seeding process, but they do not propagate throughout the entire crystal because their propagation or extension directions are restricted to the basal plane, almost normal to the growth direction. Therefore, the high density of BPDs in the top and middle portions of SiC crystals cannot be explained by the aforementioned mechanisms, and the causes of the BPDs observed in these portions remain poorly understood.

A plausible explanation is that BPDs are nucleated at the growth front (growing crystal surface) and then incorporated into the growing crystal. In general, defect formation at the growth front is closely related to the shape and morphology of the growing crystal surface; the crystal shape determines the magnitude and distribution of the thermoelastic stresses imposed on the grown crystals [13–16], and the surface morphology at the growth front largely affects the defect formation kinetics. Therefore, control of these growth parameters is crucial to obtain high-quality SiC single crystals.

In Section 1.2, I discuss the BPD formation during the PVT growth of 4H-SiC crystals. SiC single crystals of the 4H polytype are the ones studied and implemented most intensively by the industry. The present author's group investigated the BPD formation by characterizing the BPD distributions at the growth front as well as inside 4H-SiC single-crystal boules grown by PVT. The investigation was focused to identify where and how BPDs are nucleated and multiplied in PVT-grown 4H-SiC crystals. As described earlier, the growth front of 4H-SiC crystals is the most plausible location where BPDs are nucleated. The growth front comprises the (000 $\bar{1}$ ) facet and its outer (non-facet [NF]) regions; they exhibit characteristic surface morphologies in terms of the step-terrace structure. The morphologies of these two regions are quite different [17, 18], and thus different defect formation kinetics would govern the defect formation on the two surface regions. Furthermore, these two regions grow into different crystal shapes; the facet is fairly flat and has a temperature distribution across the surface during PVT growth [18], whereas the non-facet regions are convex-shaped toward the growth direction and are assumed to be roughly isothermal during growth [19]. The degree of the convexity of the growth front is also a crucial parameter for defect formation during the PVT growth of SiC. As such, investigating the crystalline properties of the facet and non-facet regions at the growth front provides valuable information about the formation of defects during the PVT growth of SiC crystals.

As described earlier in this section, another relevant issue for dislocation formation during the PVT growth of 4H-SiC crystals is the seeding process. In general, the seeding process, namely, how crystal growth is initiated on the seed crystal, is a key issue for reproducible growth of high-quality single crystals. This is also true for the PVT growth of 4H-SiC single crystals, and thus, establishing a well-controlled seeding process for the PVT growth of SiC is necessary for obtaining high-quality 4H-SiC bulk single crystals. Several authors have tried to reveal the growth mode and the defect formation process during the initial stage of PVT growth [10–12, 20–25]. However, detailed knowledge about the seeding process of SiC PVT growth remains lacking, and further intensive study is required to explore

this important technological issue in SiC PVT growth. An obstacle to investigating the seeding process of SiC PVT growth is that defect formation occurs within a very narrow range near the interface between the seed and grown crystal, and this greatly hinders detailed observations and analyses of the defect formation at the interface.

Another reason why it is difficult to study the defect formation at and near the grown-crystal/seed interface is the complexity of causes of defect formation during the initial stage of SiC PVT growth, such as thermoelastic stress [10, 12], growth kinetics [10, 11, 21], surface conditions of the seed crystal [20], and nitrogen doping enrichment near the grown-crystal/seed interface [12, 22–25]. Section 1.3 is dedicated to this issue, and recent studies of the dislocation formation at the grown-crystal/seed interface during PVT growth of 4H-SiC crystals are described. Slightly off-oriented  $(000\bar{1})$  wafers containing the beveled interface between the grown crystal and seed crystal were prepared, which revealed a characteristic dislocation structure formed at the interface and indicated the important role of vacancy injection during the initial stage of the PVT growth of 4H-SiC crystals.

In Section 1.4, I summarize this chapter and draw some conclusions.

## 1.2 Formation of Basal Plane Dislocations During PVT Growth of 4H-SiC Crystals

### 1.2.1 Plan-View X-ray Topography Observations of Growth Front

Figure 1.1 shows schematically (a) the PVT growth reactor of 4H-SiC crystals and (b) the scheme for preparing the top portion of the grown crystal with the  $(000\bar{1})$  facet and a 4H-SiC  $(1\bar{1}00)$  or  $(11\bar{2}0)$  wafer sliced vertically along the growth direction from a 4H-SiC single crystal. The crystal was grown on an on-axis or off-oriented 4H-SiC  $(000\bar{1})$ C seed crystal. The vertically sliced  $(1\bar{1}00)$  or  $(11\bar{2}0)$  wafer consisted of two

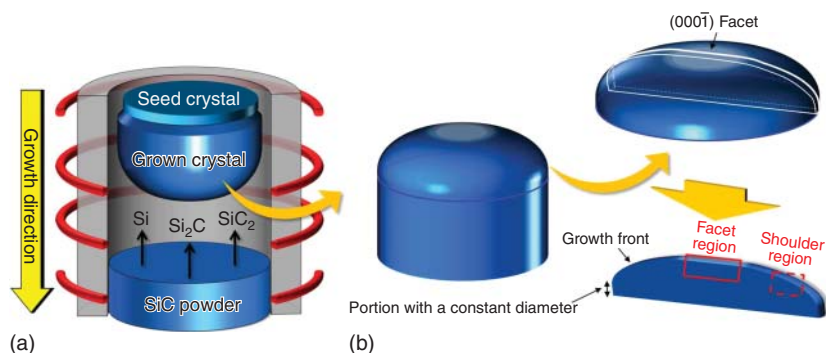


**Figure 1.1** Schematics of (a) physical vapor transport (PVT) growth reactor and (b) preparation scheme of top portion of grown crystal with  $(000\bar{1})$  facet and a 4H-SiC  $(1\bar{1}00)$  or  $(11\bar{2}0)$  wafer sliced vertically in the growth direction from a 4H-SiC single-crystal boule grown on a 4H-SiC  $(000\bar{1})$ C seed crystal. The areas in the wafer examined by transmission X-ray topography are indicated by red open rectangles. Source: Nakano et al. [26]. © 2019, Elsevier.

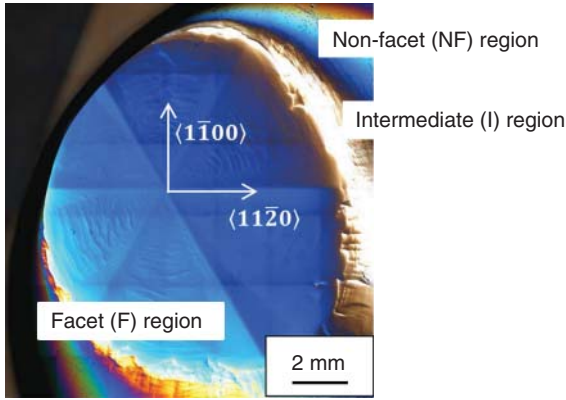


**Figure 1.2** Differential interference contrast (DIC) optical microscopy image of growth front of nitrogen-doped ( $\text{mid-}10^{18} \text{ cm}^{-3}$ ) 4H-SiC single-crystal boule examined in this study. The growth front consists of three distinct morphological regions, namely, the (000 $\bar{1}$ )C facet (F) and non-facet (NF) regions and the intermediate (I) region between them (after [27]). Source: Sonoda et al.

portions that are classified from the perspective of crystal growth. One was accompanied by the growth front that showed a domed shape (convex toward the growth direction). In this portion, crystal growth occurred during PVT growth. The other portion contained the side surfaces of the crystal, on which there was nominally no crystal growth, and thus it had a constant diameter.

Figure 1.2 shows a differential interference contrast (DIC) optical microscopy image of the growth front of a nitrogen-doped ( $\text{mid-}10^{18} \text{ cm}^{-3}$ ) 4H-SiC boule examined by Sonoda et al. [27]. The figure reveals that the growth front of the nitrogen-doped 4H-SiC single-crystal boule comprised three distinct morphological regions, namely, (i) the (000 $\bar{1}$ )C facet region (denoted as F in the figure), (ii) the non-facet (NF) region, and (iii) the intermediate (I) region between F and NF. The facet region exhibited hexagonal symmetry comprising six vicinal (000 $\bar{1}$ )C surfaces tilted toward the  $\langle 1\bar{1}00 \rangle$  direction. The vicinal surfaces were separated by six crystallographically equivalent ridges extending along the  $\langle 11\bar{2}0 \rangle$  direction. The non-facet region exhibited macroscopically smooth morphology, and the convexity of the region varied depending on the growth conditions, particularly, the temperature distribution in the growth cell. The intermediate region was arranged on the perimeter of the facet region, was narrow, and exhibited a macroscopically slightly rough morphology.

Figure 1.3 shows reflection X-ray topographs of the growth front of a nitrogen-doped 4H-SiC boule in the diffraction conditions (a)  $\mathbf{g} = 11\bar{2}8$  and (b)  $1\bar{1}07$ , obtained by Sonoda et al. [27]. In the topographs, the boundaries of the facet, intermediate, and non-facet regions are marked by dashed lines. Both topographs contain relatively intense linear contrasts extending roughly along the  $\langle 1\bar{1}00 \rangle$  direction; some of them are marked with open triangles in the topographs. They correspond to low-angle grain boundaries consisting of threading edge dislocations (TEDs) penetrating the crystal along the  $c$ -axis. Small dot-like contrasts were also observed in both topographs. They had two possible origins, namely, TSDs and TEDs, but were ascribed to TSDs based on their estimated density ( $\sim 10^3 \text{ cm}^{-2}$ ). As shown in Figure 1.3, no marked difference in the defect structure was found among the three regions of the as-grown surface, namely, the facet, intermediate,

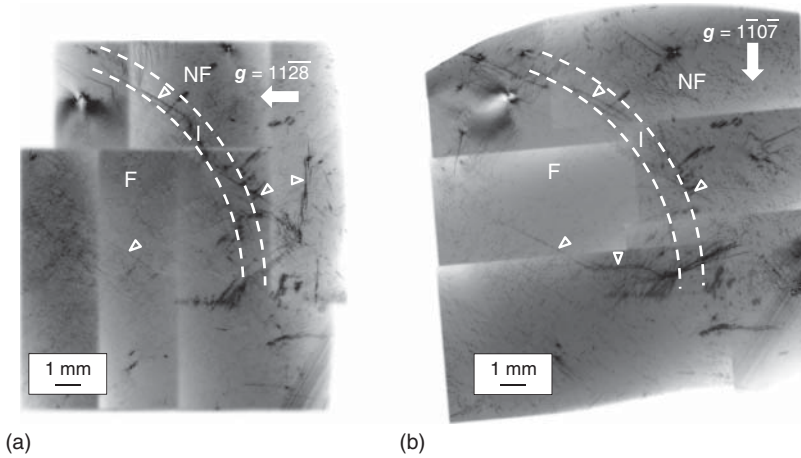


**Figure 1.3** Reflection X-ray topographs from the three regions at the growth front of a PVT-grown 4H-SiC crystal. The diffraction vector was (a)  $11\bar{2}8$  and (b)  $1\bar{1}0\bar{7}$ . In the topographs, the facet, non-facet, and intermediate regions are denoted as F, NF, and I, respectively, and their boundaries are marked by dashed lines. Source: Sonoda et al. [27].

and non-facet regions, implying that the faceted growth front hardly affects the formation of extended defects during PVT growth of 4H-SiC boules.

The topographs with diffraction vectors  $\mathbf{g} = 11\bar{2}8$  and  $1\bar{1}0\bar{7}$  shown in Figure 1.3a,b exhibit slightly different image textures. This is thought to be due to BPDs existing in the crystal portion just beneath the as-grown surface of the boule. BPDs, which have Burger vectors within the basal plane, are out of contrast when the diffraction vector is perpendicular to their Burgers vector, and thus, the two topographs taken with different diffraction vectors exhibit slightly different contrast patterns (image textures).

Figure 1.4 shows enlarged X-ray topographs for more detailed investigation of the dislocation structure underneath the facet and near-facet regions [27]. In the figure, wider-area topographs (Figure 1.4a,c) are also presented, in which the  $(000\bar{1})$  facet region is marked by a white circle, and the positions at which the enlarged X-ray topographs (Figure 1.4b,d) were taken are indicated by open squares. The topographs shown in Figure 1.4a,b were taken with the diffraction vector  $\mathbf{g} = 11\bar{2}8$ , whereas those in Figure 1.4c,d were taken in the diffraction vector  $\mathbf{g} = 1\bar{1}0\bar{7}$ . Figure 1.4b,d was acquired from the same area in the as-grown crystal surface of a 4H-SiC single-crystal boule (indicated by open squares in Figure 1.4a,c). In Figure 1.4b, both TSDs and BPDs were observed; they are indicated by closed and open triangles, respectively. By contrast, only TSDs were detected in Figure 1.4d in which BPDs exhibited no distinct contrast because the diffraction vector was set perpendicular to their Burgers vectors. These observations indicate that at this particular region of the grown crystal, most BPDs had the same Burgers vector, which implies that they arose from the same cause during the PVT growth process.

In Figure 1.4b, note that many of the observed BPDs seem to emanate from TSDs. Sonoda et al. examined other areas on the as-grown surface and found similar cases of BPDs emanating from TSDs [27]. These results suggest that the existence of

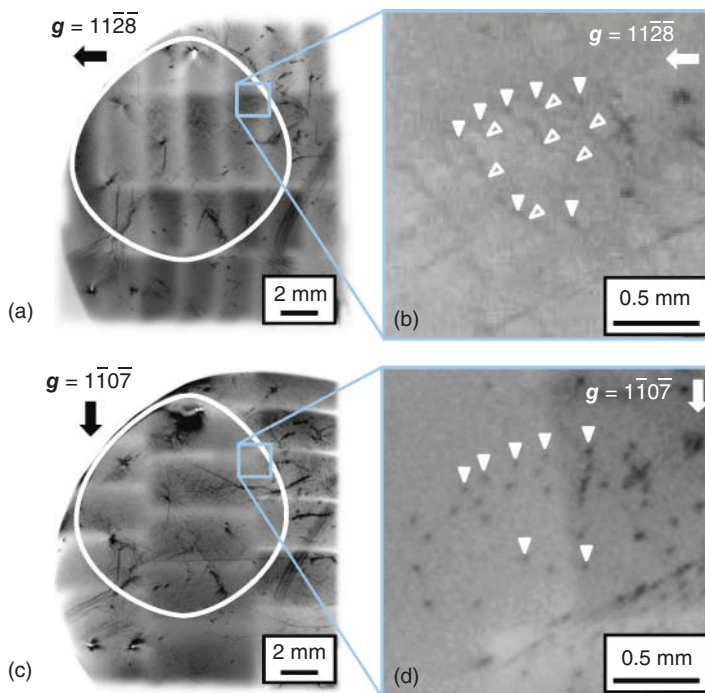


**Figure 1.4** Reflection X-ray topographs of the growth front in the diffraction conditions (a)  $g = 11\bar{2}8$  and (c)  $1\bar{1}0\bar{7}$ . (b, d) Enlarged X-ray topographs of the areas indicated by open squares in (a, c), respectively. In (b, d), some of the dot-like and line contrasts due to threading screw dislocations (TSDs) and basal plane dislocations (BPDs) are marked by closed and open triangles, respectively. Source: Sonoda et al. [27].

TSDs is related to the BPD formation at the growth front, and TSDs intersecting the growing crystal surface would induce the nucleation of BPDs at the surface during PVT growth of 4H-SiC boules. The mechanism is yet to be clarified, but the elastic interaction between TSDs and the growing crystal surface would play a crucial role in this phenomenon. In this respect, Wang et al. reported an important result that is helpful when considering the origin of this phenomenon [28]. They found that BPDs existing in commercially available 6H-SiC substrates connect or emanate from micropipes (super screw dislocations), comprising dislocation networks in the substrates. Similar BPD structures have also been reported in 4H-SiC epitaxial layers [29]. Micropipes and TSDs extending along the  $c$ -axis in an infinite crystal do not have a shear stress component parallel to the basal plane, and hence, they could not be the cause of BPDs in an infinite crystal. However, in a finite crystal, they interact elastically with the free surface, and the resultant surface relaxation due to the image force effect of dislocations [30] can provide a shear stress parallel to the basal plane. Compared to micropipes, TSDs provide lower shear stress because of their relatively smaller Burgers vector. However, the Burgers vector of TSDs would be still large enough for them to provide a shear stress exceeding the critical resolved shear stress for BPD formation at the PVT growth temperature (2300–2400 °C) and

nucleate BPD loops and/or half loops at the growing crystal surface during PVT growth of 4H-SiC crystals.

Another important finding made in the X-ray topographs shown in Figures 1.3 and 1.4 is that the density of BPDs in the facet and near-facet regions of the as-grown crystal is significantly lower than the typical BPD densities in commercially available 4H-SiC substrates. The densities of BPDs in 4H-SiC substrates are typically  $10^4$ – $10^5$   $\text{cm}^{-2}$  [31, 32] and of the order of  $10^3$   $\text{cm}^{-2}$  for state-of-the-art 4H-SiC substrates [33]. By contrast, the estimated BPD density in the facet and near-facet regions of the crystal was less than  $10^3$   $\text{cm}^{-2}$ . Sonoda et al. also examined two other 4H-SiC boules and found similar BPD densities in the crystal portion just beneath the facet and near-facet regions of the boules, although 4H-SiC substrates sliced out from the portions of the boules far from the growth front had typical BPD densities ( $10^4$ – $10^5$   $\text{cm}^{-2}$ ) [27]. These results indicate that although BPDs could nucleate at the growing crystal surface, they hardly multiply in the facet and near-facet regions of PVT-grown 4H-SiC boules.

### 1.2.2 Cross-Sectional X-ray Topography Observations of Growth Front

To examine in more detail the BPD formation at the growth front, cross-sectional X-ray topography observations of PVT-grown 4H-SiC boules were performed [27]. The two portions in a vertically sliced wafer examined by transmission X-ray topography are illustrated schematically by open rectangles in Figure 1.1b. The solid-line rectangle corresponds to a portion right beneath the facet, whereas the dashed-line rectangle corresponds to a crystal portion near the shoulder region of the grown front.

Figure 1.5a shows a cross-sectional transmission X-ray topograph for the diffraction condition  $\mathbf{g} = 11\bar{2}0$  of the portion right beneath the  $(000\bar{1})$  facet, obtained by Sonoda et al. [27]. The topograph shows several dark vertical band and line contrasts, which correspond to low-angle boundaries and threading dislocations, respectively, penetrating the boule along the growth direction ( $c$ -axis). In addition to these vertical band and line contrasts, a number of horizontal line contrasts are also observed in the topograph. Figure 1.5b shows an enlarged topograph of the portion indicated by an open rectangle in Figure 1.5a. In Figure 1.5b, some of the horizontal line contrasts are marked by open triangles. The  $\mathbf{g} \cdot \mathbf{b}$  contrast analysis revealed that these contrasts were caused by BPDs in the boule. Note here that a portion very close to the as-grown surface (facet), marked by a double-headed arrow in Figure 1.5b, is almost free of BPDs. This implies that BPDs hardly multiply in the facet and near-facet regions of the grown boule during PVT growth of 4H-SiC, which agrees well with the results of the plan-view X-ray topography observations shown in Figures 1.3 and 1.4.

Figure 1.5a also reveals that a number of BPDs exist in crystal portions distant from the growth front. This is consistent with the fact that 4H-SiC substrates prepared from these portions contain a high density of BPDs ( $10^4$ – $10^5$   $\text{cm}^{-2}$ ). An important question here is where they came from. To clarify this point, a series of X-ray topographs (not shown) was taken from the center to the edge of the boule, and it was found that many BPDs extended continuously toward the edge of the

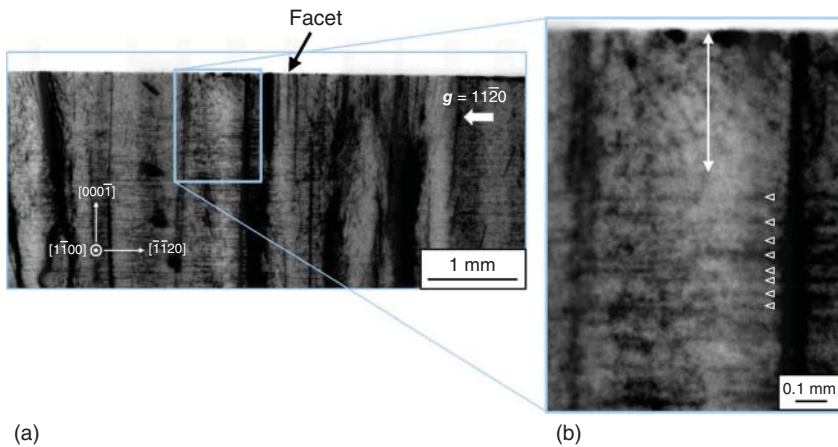
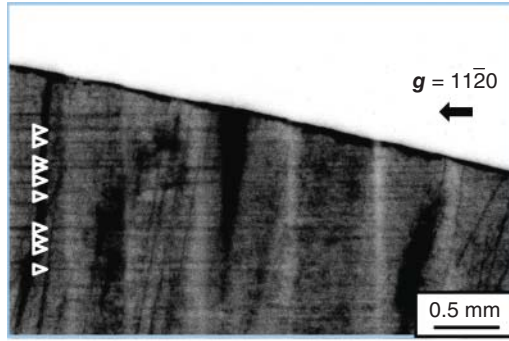


**Figure 1.5** Cross-sectional X-ray topographs for diffraction condition  $g = 11\bar{2}0$  of a crystal portion right beneath the  $(000\bar{1})$  facet of a PVT-grown 4H-SiC boule. (b) An enlarged topography image of the portion indicated by an open rectangle in (a). In (b), some of the horizontal line contrasts caused by BPDs are marked by open triangles. Source: Sonoda et al. [27].

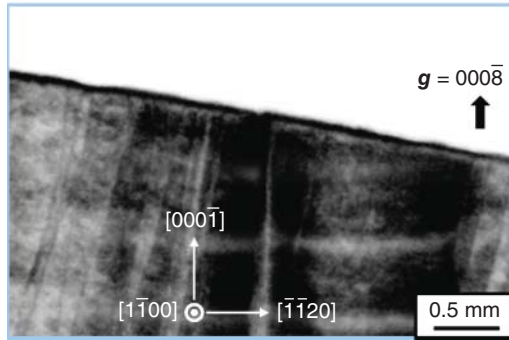
boule and terminated at the shoulder region of the growth front. Figure 1.6 shows X-ray topographs of a crystal portion underneath the shoulder region of a 4H-SiC single-crystal boule [27]. The location of the crystal portion in the boule is indicated by a dashed-line rectangle in Figure 1.1b. Figure 1.6a,b shows X-ray topographs of the portion for the diffraction conditions  $g = 11\bar{2}0$  and  $000\bar{8}$ , respectively. As shown in Figure 1.6a ( $11\bar{2}0$  topograph), a number of horizontal line contrasts extend along the basal plane; some of them are marked by open triangles in the figure. As shown in the figure, the horizontal line contrasts terminate at the as-grown surface of the boule. By contrast, they are lost in Figure 1.6b ( $000\bar{8}$  topograph), and thus, they were ascribed to BPDs. To elaborate the BPD formation process, Sonoda et al. examined the other ends of these horizontal line contrasts and found that many of them terminated within the crystal at positions roughly below the facet. They observed a similar distribution of BPDs in the other half of the wafer and thus inferred that BPDs were nucleated at the shoulder region of the growth front and extended toward the inside of the grown boule via dislocation glide and multiplication processes during PVT growth. By contrast, such BPD glide and multiplication processes hardly occur in the facet and near-facet regions, resulting in a very low BPD density in the crystal portion right beneath these regions.

These BPD behaviors are illustrated more clearly in a wider-area transmission X-ray topograph shown in Figure 1.7, where the BPD-free crystal portion right beneath the facet and near-facet regions is bounded by a dashed line. In the figure, some of the BPDs extending along the basal plane in the grown crystal are indicated by open triangles. As shown in the figure, the boundary between the BPD-free portion and the other portions has a characteristic “round neck” shape that indicates that the BPD distribution in PVT-grown 4H-SiC crystals is controlled

**Figure 1.6** Cross-sectional X-ray topographs for diffraction conditions (a)  $g = 11\bar{2}0$  and (b)  $000\bar{8}$  of a crystal portion underneath the shoulder region of the growth front of a PVT-grown 4H-SiC crystal, whose location in the crystal is indicated by a dashed line rectangle in Figure 1.1b. In (a), a number of horizontal line contrasts due to BPDs are observed; some of them are marked by open triangles. Source: Sonoda et al. [27].



(a)



(b)

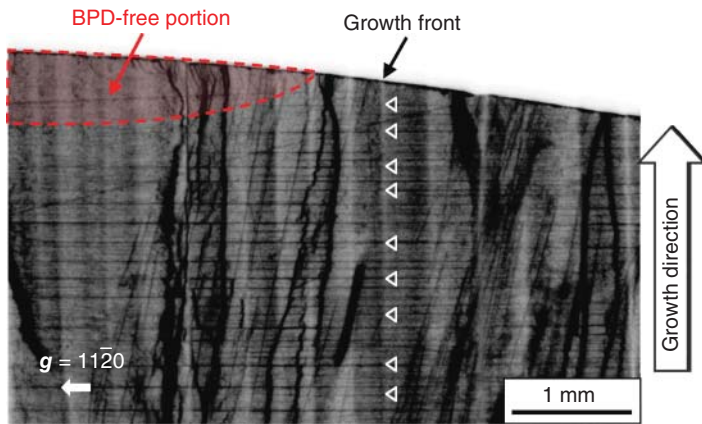


**Figure 1.7** Wider-area transmission X-ray topograph for diffraction condition  $g = 11\bar{2}0$ , which shows the existence of an almost BPD-free crystal portion right beneath the facet and near-facet regions at the growth front. Some of the BPDs extending along the basal plane are indicated by open triangles. The “round-neck” boundary between the BPD-free portion and the other portions is indicated by a dashed line.

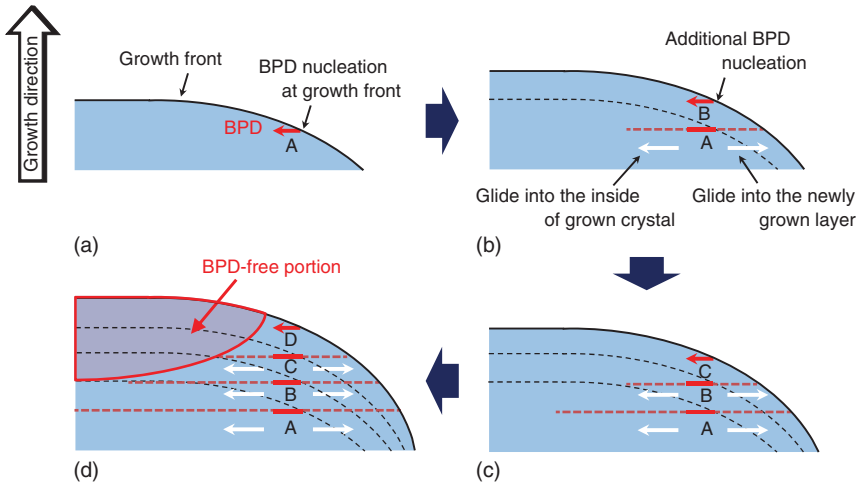


**Figure 1.8** Schematics of temporal change of BPD distribution in a 4H-SiC crystal during PVT growth. (a) Nucleation of BPDs at the shoulder region of the grown crystal, and (b) glides of BPDs into the crystal and also toward the growth front of the crystal through the newly grown layer, together with the nucleation of additional BPDs at the growth front. (c) Repetition of processes (a, b) at the growth front of the newly grown layer during PVT growth, and (d) resulting round-neck distribution of BPDs due to the different glide distances of BPDs nucleated at different times in the PVT growth process.

by the BPD nucleation at the shoulder region of the grown crystal. This important conclusion was drawn by considering the glide and multiplication of BPDs after they nucleate at the shoulder region. These processes are illustrated in Figure 1.8, which shows schematically how the BPD distribution in a 4H-SiC crystal changes with time during PVT growth. Figure 1.8a shows the nucleation of BPDs at the shoulder region of a PVT-grown 4H-SiC crystal, and as the PVT growth proceeds, the nucleated BPDs glide into the grown crystal and also extend toward the growth front through the newly grown layer (Figure 1.8b). At this stage, additional BPDs nucleate at the growth front of the newly grown layer, and the aforementioned processes are repeated during PVT growth (Figure 1.8c), resulting in the round-neck distribution of BPDs (Figure 1.8d) because of the different glide distances of BPDs nucleated at different stages of the PVT growth process.

The BPD formation at the shoulder region of the PVT-grown SiC crystals coincides well with numerical results by Gao and Kakimoto [16]. They conducted three-dimensional numerical modeling of BPD multiplication in 4H-SiC bulk crystals. They calculated the resolved thermoelastic shear stresses on the basal plane during PVT growth of 4H-SiC and then substituted them into the Alexander–Hassen model to obtain the BPD distribution in PVT-grown 4H-SiC crystals. Their results showed that the shape of the growth front is key for BPD multiplication, with a largely convex growth front giving rise to a high resolved shear stress on the basal plane at the shoulder region of 4H-SiC boules during PVT growth, thus introducing many BPDs from the region. Their results also suggested that BPD multiplication occurs mainly in the crystal growth stage of the PVT growth process rather than in

the cooling stage. I believe that some irregularities at the growing crystal surface, such as TSD outcrops, become the nucleation sites of BPDs and lead to dislocation multiplication if a sufficiently high thermoelastic shear stress is imposed at these sites during PVT growth. The observed characteristic distribution of BPDs in the growth-front portion of 4H-SiC single-crystal boules corroborates this assumption.

### 1.2.3 Characteristic BPD Distribution in PVT-Grown 4H-SiC Crystals

In Section 1.2.2, it was revealed that many BPDs are introduced from the shoulder region of 4H-SiC crystals grown in the  $[000\bar{1}]$  direction. However, it remains unclear how these BPDs behave in the crystals after their introduction. To clarify their behaviors, X-ray topography and Raman microscopy were conducted on a vertically sliced 4H-SiC ( $11\bar{2}0$ ) wafer, which is shown schematically in Figure 1.1b. Figure 1.9a,b shows transmission X-ray topographs of a 4H-SiC ( $11\bar{2}0$ ) wafer for the diffraction conditions  $\mathbf{g} = 000\bar{8}$  and  $1\bar{1}00$ , respectively, obtained by Nakano et al. [26]. The area where the topographs were taken is indicated schematically by a red open square in Figure 1.9c. As shown in the topographs, strong horizontal line contrasts are observed in Figure 1.9b (diffraction vector:  $1\bar{1}00$ ), which almost diminish in Figure 1.9a (diffraction vector:  $000\bar{8}$ ). By contrast, in Figure 1.9a, line contrasts extending along the  $c$ -axis (growth direction) are observed, which correspond to TSDs. In Figure 1.9a, broad band contrasts are also observed at the positions where the strong horizontal line contrasts are observed in Figure 1.9b. The strong horizontal line contrasts observed in Figure 1.9b were caused by either BPDs or basal plane stacking faults in the crystal. To clarify the origin of the strong horizontal line contrasts observed in Figure 1.9b, Nakano et al. performed defect-selective etching

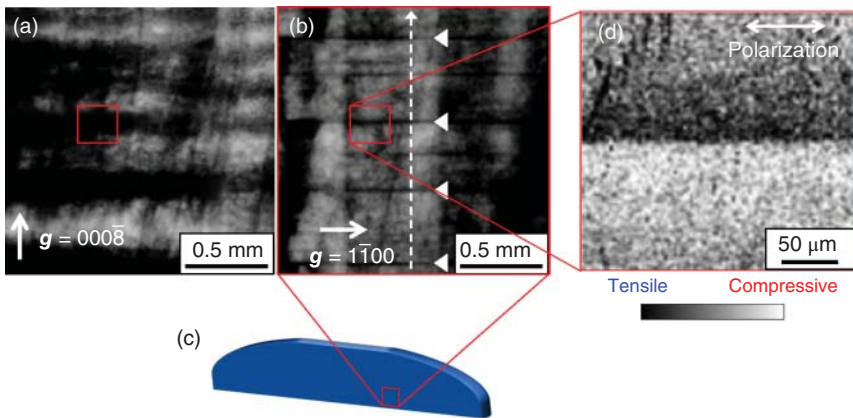


**Figure 1.9** Transmission X-ray topographs for diffraction conditions (a)  $\mathbf{g} = 000\bar{8}$  and (b)  $1\bar{1}00$  of a vertically sliced 4H-SiC ( $11\bar{2}0$ ) wafer. In (c), the area in the wafer examined by transmission X-ray topography is shown as an open rectangle. (d) Raman microscopy image of a layer with a high density of BPDs (bunched BPDs). The white dashed arrow in (b) indicates the points and direction where the variations of the  $E_2$  mode peak position and the  $a$ -lattice constant (Figure 1.10) were measured. Source: Nakano et al. [26]. © 2019, Elsevier.

(molten KOH etching) and found that they were caused by a high density of BPDs; Nakano et al. referred to this type of BPDs as “bunched BPDs” [26]. Note here that such bunched BPDs are arranged almost periodically along the growth direction in the grown crystal, as revealed in Figure 1.9b, where some of the bunched BPDs are indicated by closed white triangles.

To examine the structure of bunched BPDs in more detail, Raman microscopy imaging of bunched BPDs was conducted. The imaged area is indicated by a red open square in Figure 1.9a,b, and the peak position of the  $E_2$  mode at  $\sim 776\text{ cm}^{-1}$  was plotted across this area with the polarization vectors of the incident and scattered light parallel to the basal plane. The obtained image is shown in Figure 1.9d, in which the light polarization is indicated by a double-headed arrow. As shown in the figure, there is a clear difference in the peak position between the upper and lower sides of bunched BPDs. In the upper side, the peak of the  $E_2$  mode shifts to a lower position, while the peak is positioned at higher wavenumbers in the lower side, implying the existence of tensile (compressive) strain in the upper (lower) side of bunched BPDs.

Figure 1.10 shows how (i) the  $E_2$  peak position and (ii) the  $a$ -lattice constant (lattice constant within the basal plane) vary in the growth direction as measured by high-resolution X-ray diffraction (HRXRD). These variations were measured along the line indicated by a white dashed arrow in Figure 1.9b. As shown in Figure 1.10a, the peak position shifted abruptly where bunched BPDs existed. The

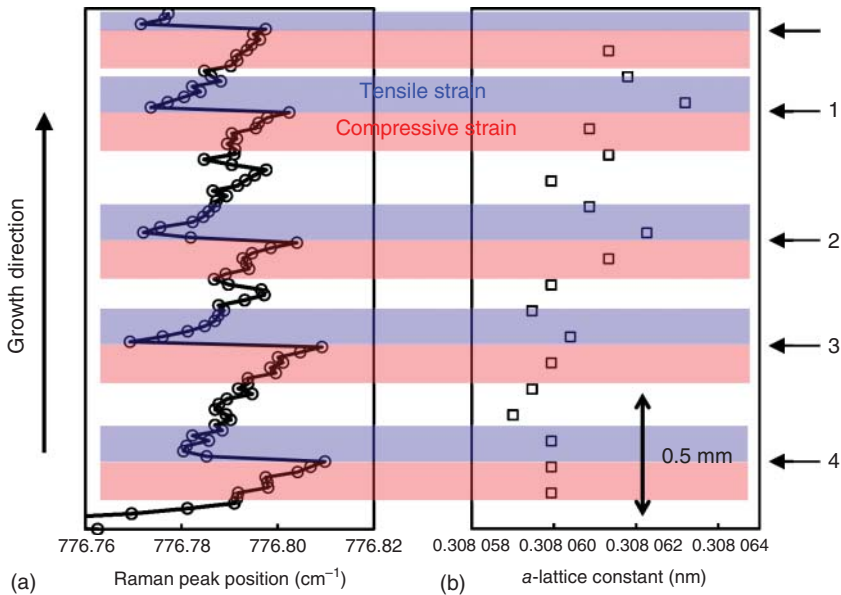


**Figure 1.10** Variations of (a) peak position of Raman-active  $E_2$  mode around  $776\text{ cm}^{-1}$  and (b) the  $a$ -lattice constant measured using HRXRD in the growth direction on a vertically sliced 4H-SiC (11 $\bar{2}$ 0) wafer. The measured points and direction are indicated by a white dashed arrow in Figure 1.9b. (a) shows clearly that abrupt shifts of the  $E_2$  peak position occurred at bunched BPDs; the positions of some of the bunched BPDs are indicated by arrows in the right-hand side of the figure (after [26]).

positions of some of the bunched BPDs are indicated by arrows in the right-hand side of Figure 1.10; those indicated by the arrows numbered from 1 to 4 correspond to the bunched BPDs indicated by closed white triangles in Figure 1.9b. The shift at bunched BPDs always occurred toward lower wavenumbers when the light beam was scanned from the bottom to the top of the grown crystal, implying that tensile strain within the basal plane always exists in the upper side of bunched BPDs [34–36]. The  $a$ -lattice constant also varied in the growth direction and increased in the upper side of bunched BPDs. This is consistent with the variation of the  $E_2$  mode peak position, and it can be concluded that the tensile strain within the basal plane existing in the upper side of bunched BPDs resulted in a larger  $a$ -lattice constant.

The aforementioned results indicate that bunched BPDs are accompanied by extra half-planes pointing toward the seed crystal. This is reasonable if bunched BPDs are introduced by the thermoelastic stress imposed on the growing crystal during the PVT growth of SiC. The SiC PVT growth process is driven primarily by the temperature gradient along the  $c$ -axis (growth direction), and thus, a high  $\sigma_{rz}$  shear stress is imposed on the growing crystal during PVT growth, where  $r$  and  $z$  denote the radial and axial directions, respectively, of the grown crystal ( $z$  is parallel to the  $c$ -axis). At typical PVT growth temperatures ( $>2300$  °C), SiC crystals deform plastically and the  $\sigma_{rz}$  shear stress is relieved considerably by the introduction of BPDs into the crystal. During the PVT growth process, a positive temperature gradient is maintained in the growth direction, and thus when the thermoelastic stress is relieved, BPDs are introduced that have extra half-planes pointing toward the seed crystal.

#### 1.2.4 BPD Multiplication During PVT Growth

To investigate in more detail how BPDs behave during the PVT growth of 4H-SiC crystals, further extended Raman microscopy imaging of bunched BPDs in the lateral direction (parallel to the basal plane) was performed. The result of the Raman microscopy imaging is shown in Figure 1.11a. The image is a two-dimensional mapping of the peak position of the  $E_2$  mode around  $776\text{ cm}^{-1}$  on a vertically sliced 4H-SiC ( $11\bar{2}0$ ) wafer. Similarly to Figure 1.9d, the peak position differs clearly between the upper and lower sides of bunched BPDs. Note in this figure that the contrast difference between the upper and lower sides of bunched BPDs varies along the basal plane. In Figure 1.11a, portions with larger and smaller contrast differences are indicated by closed and open triangles, respectively. Nakano et al. found that the observed variation of the contrast difference (magnitude of the abrupt shift of the  $E_2$  mode peak position at bunched BPDs) along the basal plane was correlated with the TSD density in the crystal [26]. Figure 1.11b shows the relationship between the contrast difference and the TSD density; the latter was estimated from the density of the line contrasts extending along the  $c$ -axis in X-ray topographs with the diffraction vector  $\mathbf{g} = 000\bar{8}$  (e.g. Figure 1.9a) at the position where the contrast difference was measured by Raman microscopy. As shown in the figure, the magnitude of the abrupt peak shift at bunched BPDs is correlated well with TSD density: as the TSD density increases, the abrupt peak shift at bunched

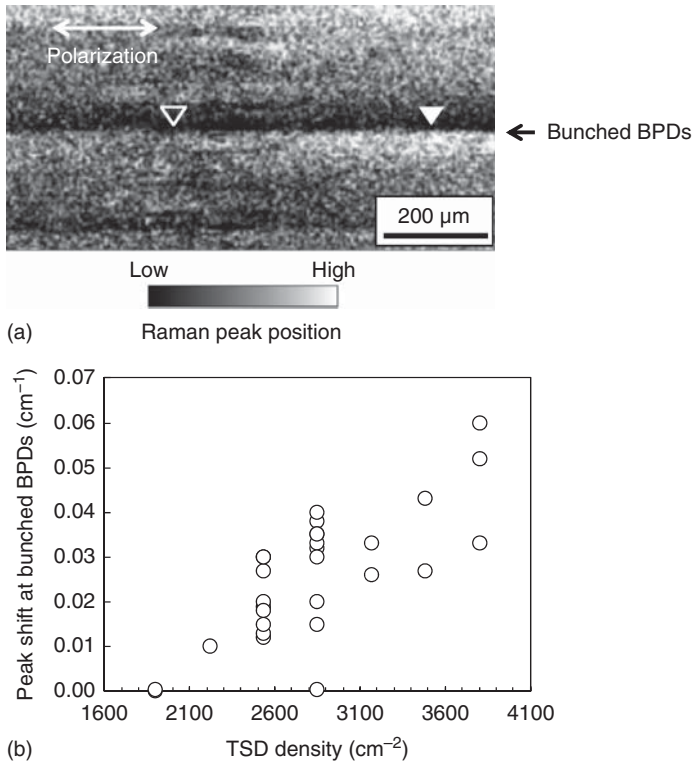


**Figure 1.11** (a) Extended Raman microscopy image of bunched BPDs along the basal plane. The image shows variation of the  $E_2$  mode peak position around bunched BPDs. The open and closed triangles in the image indicate portions that exhibited smaller and larger abrupt peak shifts, respectively, at the bunched BPDs. (b) A positive correlation between the magnitude of the abrupt peak shift at the bunched BPDs and the TSD density. Source: Nakano et al. [26]. © 2019, Elsevier.

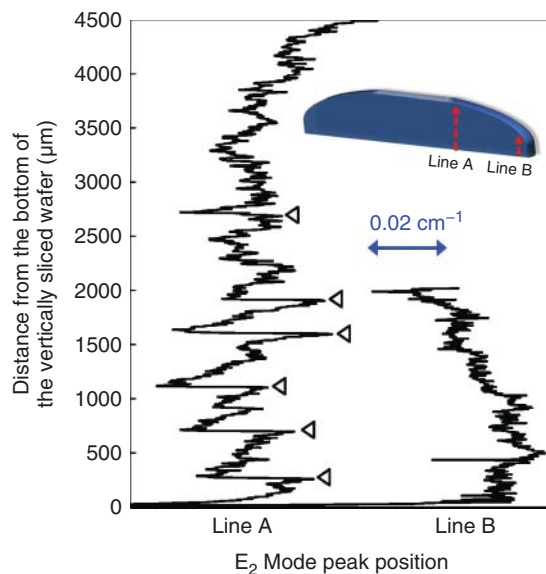
BPDs becomes larger, which implies that the TSD and BPD densities in PVT-grown 4H-SiC crystals are correlated positively.

Ohtani et al. [37] reported a similar positive correlation between the TSD and BPD densities in PVT-grown 4H-SiC crystals. They conducted defect-selective etching using molten KOH to estimate the TSD and BPD densities in PVT-grown 4H-SiC crystals and found that the BPD density increased with the TSD density in the crystals. They ascribed this positive correlation to BPD multiplication around TSDs. Temperature gradients in 4H-SiC crystals during PVT growth cause BPDs to glide on the basal plane and cut through a forest of TSDs extending along the  $c$ -axis in the crystals. After crossing TSDs, BPDs have super jogs parallel to the  $c$ -axis, which are immobile and anchored in the crystal. When the BPDs glide further under thermoelastic stress during PVT growth and/or post-growth cooling, the well-known Frank-Read-type BPD multiplication occurs, and consequently the BPD density increases significantly around TSDs [32, 38]. This is why the BPD and TSD densities are correlated positively in 4H-SiC crystals.

As described in Section 1.2.3, BPDs have a characteristic distribution in the growth direction in PVT-grown 4H-SiC crystals; layers exist with a high density of BPDs (bunched BPDs) arranged almost periodically in the growth direction. As for the BPD formation in PVT-grown 4H-SiC crystals, it was also revealed in Section 1.2.2 that a number of BPDs are introduced from the shoulder region of the grown crystal during PVT growth. In this respect, it is noteworthy that bunched BPDs were observed relatively far from the shoulder region of the grown crystal. Given these results, an important question arises as to where and when bunched BPDs are introduced in crystals. A possible mechanism is that bunched BPDs are introduced from the side surfaces of grown crystals. The constant-diameter portion of a grown crystal has side surfaces that are located very close to the crucible inner walls, and under certain growth conditions, they can come into contact with the walls during PVT growth or cooling because of the different coefficients of thermal expansion of SiC and graphite. Therefore, the side surfaces of the grown crystal could be subject to high stress during PVT growth, thereby introducing a number of BPDs from the side surfaces. However, X-ray topography observations of a crystal portion near the side surfaces of 4H-SiC grown crystals revealed no bunched BPDs near the side surfaces [26].

To examine further the origin of bunched BPDs, further extended Raman microscopy analysis was performed in the growth direction. Figure 1.12 shows how the  $E_2$  peak position varies in the growth direction [26]. The variations were measured along two lines, one that started from the bottom of a vertically sliced wafer and ended near the (000 $\bar{1}$ ) facet region at the growth front (denoted by line A) and one that was close to the side surface (edge) of a grown crystal (denoted by line B). The locations of these two lines (lines A and B) in a vertically sliced (11 $\bar{2}$ 0) wafer are indicated schematically by dashed arrows in the inset of Figure 1.12. As shown in Figure 1.12, the  $E_2$  peak position often shifted abruptly along line A;

**Figure 1.12** Variations of  $E_2$  mode peak position in growth direction measured in the near-facet (line A) and edge (line B) portions of a vertically sliced 4H-SiC (11 $\bar{2}$ 0) wafer. The locations of the two measured portions (lines A and B) in the wafer are indicated by dashed arrows in the inset figure. Source: Nakano et al. [26]. © 2019, Elsevier.



some of the shifts are indicated by open triangles in the figure. By contrast, no such abrupt shifts were seen along line B. Note here that the abrupt shift intensified as the measured point approached the bottom of the vertically sliced wafer, implying that the BPD density in bunched BPDs increases gradually toward the seed crystal. Such an increase in BPD density toward the seed crystal is reasonable if bunched BPDs are introduced from the growth front (top surface of the growing crystal) during PVT growth. Once bunched BPDs are introduced from the growth front, their BPD density increases gradually as the growth proceeds, this being because the total duration of thermoelastic stress imposed on the growing crystal increases with the growth time.

The abovementioned discussions combine to give the important conclusion that bunched BPDs or their nuclei would be introduced at the growth front (domed surface) but hardly so from the side surfaces of grown crystals. The most plausible location where bunched BPDs are introduced would be the shoulder region of the growing crystal. Gao and Kakimoto [16] showed theoretically that the domed shape of the growth front gives rise to a high resolved shear stress on the basal plane in the shoulder region of the grown crystal during PVT growth of 4H-SiC, thus causing many BPDs to be introduced from that region. This theoretical prediction was subsequently confirmed experimentally by Sonoda et al. using X-ray topography [27]. The aforementioned results of Nakano et al. [26] indicate that the shoulder region of the growing crystal is a major source of BPDs, including bunched BPDs or their nuclei, and the BPDs introduced from that region would determine the distribution of BPDs throughout PVT-grown 4H-SiC crystals.

### 1.3 Dislocation Formation During Initial Stage of PVT Growth of 4H-SiC Crystals

#### 1.3.1 Preparation of 4H-SiC Wafers with Beveled Interface Between Grown Crystal and Seed Crystal

In this section, I describe the formation of dislocations at the grown-crystal/seed interface of PVT-grown 4H-SiC crystals. As described in Section 1.1, most threading dislocations in PVT-grown 4H-SiC crystals form during the initial stage of PVT growth, and thus, it is essential to control the growth initiation to obtain high-quality 4H-SiC crystals. To reveal the processes for dislocation formation in the initial stage of 4H-SiC PVT growth, Shioura et al. [39] prepared 4H-SiC wafers containing a beveled interface between the grown crystal and the seed crystal and used them to examine the detailed distribution of crystallographic defects at and near the interface. Figure 1.13 shows schematics of the slicing geometry of a 4H-SiC crystal grown on a  $4^\circ$  off-oriented  $(000\bar{1})$  seed crystal, providing a  $1.5^\circ$  off-oriented  $(000\bar{1})$  wafer, which has a beveled interface between the grown crystal and seed crystal [39]. Figure 1.13a is a schematic side view of a nitrogen-doped 4H-SiC crystal grown on a  $4^\circ$  off-oriented  $(000\bar{1})$  seed crystal and a slightly off-oriented ( $1.5^\circ$  off-oriented approximately toward  $[11\bar{2}0]$ )  $(000\bar{1})$  wafer sliced out from the grown crystal, while

**Figure 1.13** Schematics of slicing geometry of a nitrogen-doped 4H-SiC crystal grown on a  $4^\circ$  off-oriented  $(000\bar{1})$  seed crystal, providing a  $1.5^\circ$  off-oriented  $(000\bar{1})$  wafer, which has a beveled interface between the grown crystal and the seed crystal. (a) Side view of grown crystal and  $1.5^\circ$  off-oriented  $(000\bar{1})$  wafer sliced out from the crystal. (b) Top view of sliced wafer. Source: Shioura et al. [39]. © 2019, Elsevier.

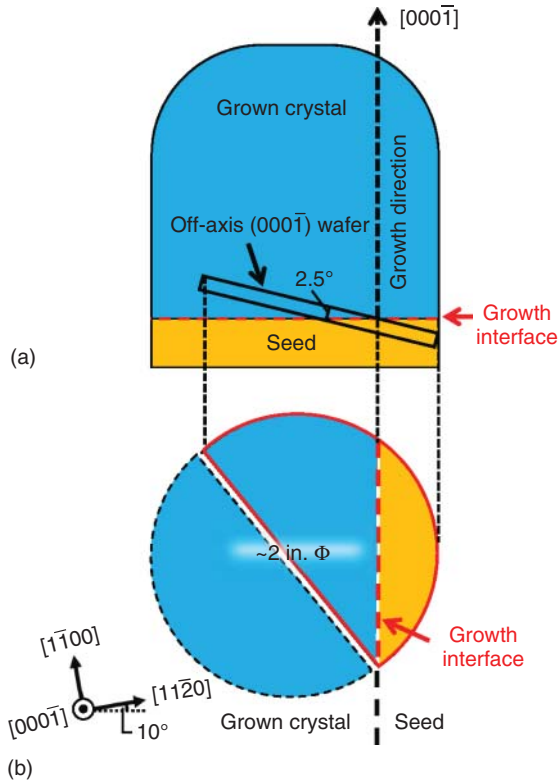
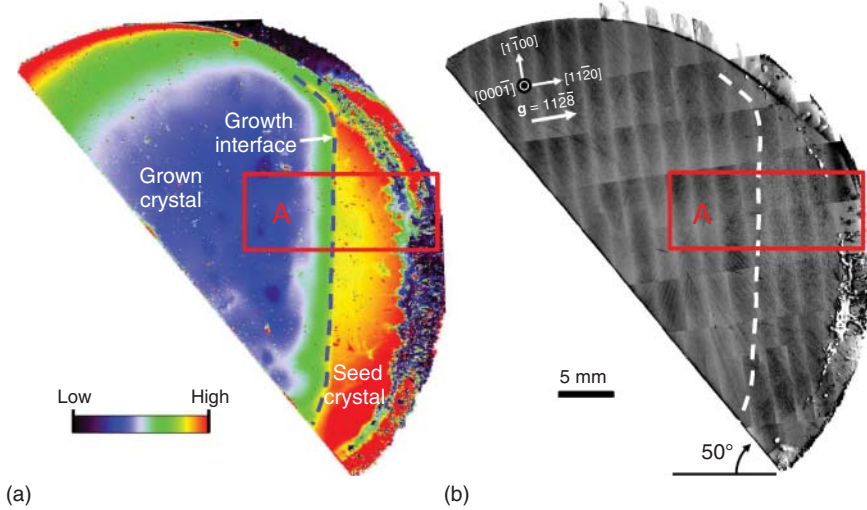


Figure 1.13b shows a top view of the sliced wafer. The angle between the wafer surface and the grown-crystal/seed interface was relatively shallow ( $2.5^\circ$ ), and thus, the defective near-interface region was substantially enlarged to facilitate detailed observations and analyses of defects at and near the interface. Shioura et al. examined this substantially enlarged interfacial region between the grown crystal and seed crystal using Raman microscopy and X-ray topography, and on the basis of the obtained results elucidated the formation mechanisms of crystallographic defects during the initial stage of PVT growth of 4H-SiC crystals [39].

### 1.3.2 Determination of Grown-Crystal/Seed Interface by Raman Microscopy

Figure 1.14 shows (a) an intensity mapping image of the whole  $1.5^\circ$  off-oriented 4H-SiC  $(000\bar{1})$  wafer containing the grown-crystal/seed interface, acquired using the intensity of the longitudinal optical phonon–plasmon-coupled (LOPC) mode around  $983\text{ cm}^{-1}$ , and (b) a reflection X-ray topograph of the wafer for the diffraction condition  $\mathbf{g} = 11\bar{2}\bar{8}$  [39]. The intensity of the LOPC mode is known to be very sensitive to the carrier (electron) concentration in 4H-SiC crystals: as the electron concentration increases, the intensity decreases rapidly [40, 41]. As shown in Figure 1.14a, the LOPC mode scattering intensity differs markedly between the seed



**Figure 1.14** (a) Raman mapping image using longitudinal optical phonon–plasmon-coupled (LOPC) mode intensity of a  $1.5^\circ$  off-oriented 4H-SiC (000 $\bar{1}$ ) wafer with a beveled interface between the grown crystal and the seed crystal, which corresponds to the upper right part of the wafer illustrated schematically in Figure 1.13b. (b) Reflection X-ray topograph of the  $1.5^\circ$  off-oriented 4H-SiC (000 $\bar{1}$ ) wafer in the diffraction condition  $g = 11\bar{2}8$ . The position of the interface between the grown crystal and seed crystal is indicated by a dashed line, and the region used for subsequent Raman microscopy and X-ray topography analyses is indicated by a red open rectangle (region A) in both (a, b). Source: Shioura et al. [39]. © 2019, Elsevier.

and grown crystal regions, and thus, their interface can be determined by Raman microscopy. Figure 1.15 shows enlarged Raman microscopy images across region A in the wafer, whose location is indicated by a red open rectangle in Figure 1.14a,b. In Figure 1.15, mapping images of (a) Raman scattering intensity, (b) peak position, and (c) width of the LOPC asymmetric peak are shown, together with their line profiles across the grown-crystal/seed interface, namely, (d) intensity, (e) peak position, and (f) peak width. As shown in Figure 1.15d, the Raman scattering intensity decreases rapidly from the point indicated by a red triangle in the figure toward the left-hand side of the figure (in the growth direction). Ohshige et al. reported that the electron concentration in PVT-grown 4H-SiC crystals increases abruptly at the grown-crystal/seed interface because of the enrichment of nitrogen donors in the crystal in its initial growth stage [23]. The rapid decrease in the scattering intensity shown in Figure 1.15d is thought to be due to the nitrogen enrichment at the grown-crystal/seed interface, and thus, using the LOPC intensity profile, the location of the interface between the grown crystal and the seed crystal can be determined reasonably as the point indicated by a red triangle in Figure 1.15d.

According to the scheme described earlier, the grown-crystal/seed interface was determined and indicated as a dashed line in Figures 1.14 and 1.15a–c [39]. In all the figures, the left-hand side of the dashed line is the grown crystal, while the right-hand side corresponds to the seed crystal.

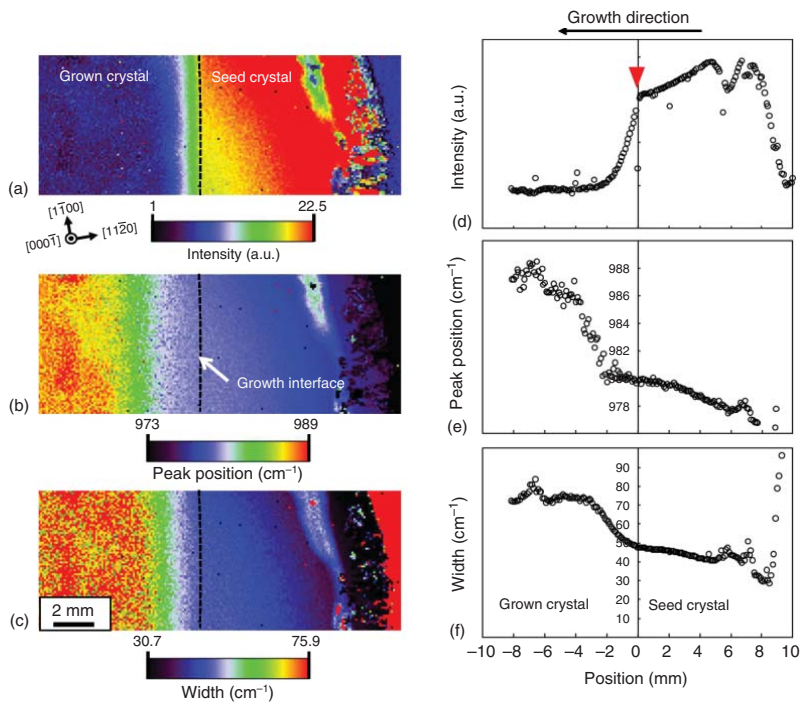


**Figure 1.15** Raman microscopy images of region A, which is indicated by a red open rectangle in Figure 1.14: (a) scattering intensity, (b) peak position, and (c) width of the asymmetric LOPC peak around  $983\text{ cm}^{-1}$ , where the position of the grown-crystal/seed interface is indicated by a dashed line in each image. The variations of the intensity, peak position, and width of the LOPC peak across the interface are shown in (d–f), respectively, where the data were averaged in the direction parallel to the grown-crystal/seed interface (after [39]). Source: Shioura et al.

### 1.3.3 X-ray Topography Observations of Dislocation Structure at Grown-Crystal/Seed Interface

To examine more clearly the defect structure near the grown-crystal/seed interface, an enlarged X-ray topograph from the interface region was taken and is shown in Figure 1.16 [39], which is a reflection X-ray topography image for the diffraction condition  $\mathbf{g} = 11\bar{2}\bar{8}$  acquired from region A indicated by a red open rectangle in Figure 1.14. The grown-crystal/seed interface determined by Raman microscopy imaging is indicated by a dashed line in Figure 1.16. The image shows the existence of widespread networks of BPDs near the grown-crystal/seed interface; some of them are marked by white triangles in Figure 1.16. Similar BPD networks have been reported by Tani et al. [24]. They conducted high-voltage transmission electron microscopy (HVTEM) observations and found that BPDs in the networks connected to each other to form cell-like structures and decomposed into stacking faults at the triple nodes of the networks. In Figure 1.16, a cell-like feature of the BPD networks formed at the grown-crystal/seed interface is also observed, and more interestingly, it was found that the networks extended considerably into the seed crystal.

Shioura et al. conducted  $\mathbf{g} \cdot \mathbf{b}$  contrast analyses of the BPD networks observed at the grown-crystal/seed interface to determine the nature of the networks [39]. The results are shown in Figure 1.17, where reflection X-ray topographs of region B, which is indicated by an open square in Figure 1.16, are shown; they were taken for the diffraction conditions (a)  $\mathbf{g} = 11\bar{2}\bar{8}$ , (b)  $\bar{1}01\bar{7}$ , (c)  $\bar{1}10\bar{7}$ , and (d)  $01\bar{1}\bar{7}$ . Figure 1.17 reveals that under each diffraction condition, some parts of the BPD networks become out of contrast; the parts that are out of contrast under each diffraction condition are indicated by white lines in each topograph. The extinction of the diffraction contrast means that the Burgers vectors associated with these parts of the BPD networks are perpendicular to the diffraction vector, and thus, the results of the  $\mathbf{g} \cdot \mathbf{b}$  contrast analyses shown in Figure 1.17 demonstrate that the BPD networks

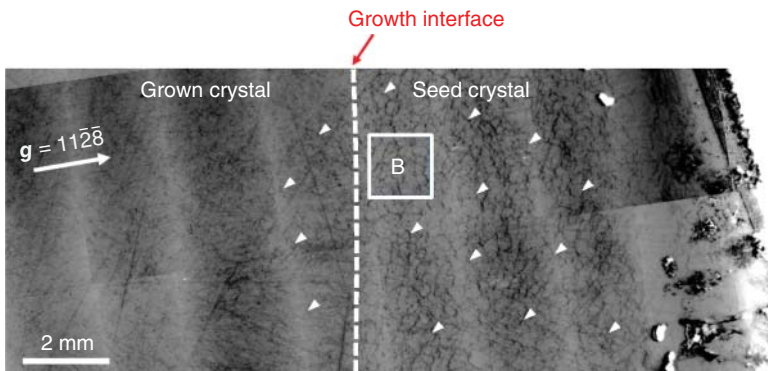


**Figure 1.16** Reflection X-ray topograph for diffraction condition  $\mathbf{g} = 11\bar{2}\bar{8}$  of region A in  $1.5^\circ$  off-oriented 4H-SiC (0001) wafer, where the position of the grown-crystal/seed interface is indicated by a white dashed line. In this figure, the region used for subsequent  $\mathbf{g} \cdot \mathbf{b}$  analyses (see Figure 1.17) is indicated by a white open square (region B). Source: Shioura et al. [39].

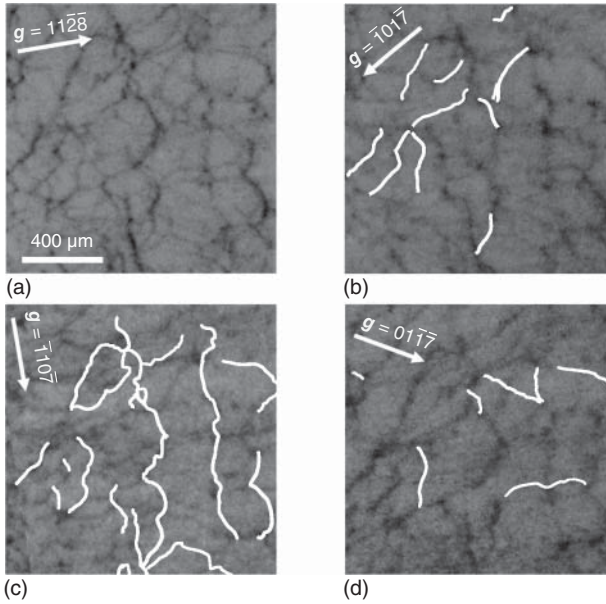


**Figure 1.17** Reflection X-ray topographs of BPD networks observed in region B of 1.5° off-oriented 4H-SiC (0001) wafer for diffraction conditions (a)  $g = 11\bar{2}8$ , (b)  $\bar{1}01\bar{7}$ , (c)  $\bar{1}10\bar{7}$ , and (d)  $01\bar{1}\bar{7}$ . The diminished parts of the BPD networks under each diffraction condition are indicated by white solid lines in each topograph. Source: Shioura et al. [39].

consist mainly of edge-type BPDs that have a Burgers vector perpendicular to the dislocation line. This result suggests that a high density of BPDs observed at the grown-crystal/seed interface would have been caused by some form of misfit stress within the basal plane imposed at the interface during the initial stage of PVT growth.

To investigate further the nature of the BPD networks, the bending of the (0001) basal plane was examined by means of measurements of the peak position shift of the  $\omega$ -scan 0008 HRXRD rocking curve across the grown-crystal/seed interface [39]. The results indicated that the (0001) basal plane in the slightly off-oriented (000 $\bar{1}$ ) wafer contained the beveled interface between the grown crystal and seed crystal bent in a concave manner in the [000 $\bar{1}$ ] growth direction, which implies that the crystal near the grown-crystal/seed interface contained extra half-planes pointing in the [0001] direction (the backside of the seed crystal).

#### 1.3.4 Formation Mechanism of BPD Networks and Their Migration into Seed Crystal

It was revealed by HRXRD measurements that there were extra half-planes pointing in the [0001] direction in the crystal near the grown-crystal/seed interface [39]. These extra half-planes are thought to be associated with the BPD networks existing near the grown-crystal/seed interface. It was also revealed that most parts of BPDs comprising the networks have an edge component, and thus, they are likely to have

been caused by misfit strain accommodated at the interface during the initial stage of SiC PVT growth.

The misfit strain within the basal plane at the grown-crystal/seed interface has two possible origins, namely, (i) nitrogen enrichment at the interface and (ii) the temperature gradient in the growth direction imposed on the growing crystal in the initial stage of PVT growth. The nitrogen enrichment at the grown-crystal/seed interface has been reported by several authors [12, 22–25]. The grown crystal was doped intentionally with nitrogen in the same concentration as the seed crystal; however, residual nitrogen impurities in the growth atmosphere and/or those adsorbed on the source powder surface could give rise to a relative enrichment of nitrogen in the crystal grown during the early stage of PVT growth. Nitrogen doping has been reported to give rise to a smaller lattice spacing [42] and also a smaller coefficient of thermal expansion [43] within the basal plane for 4H-SiC crystals; thus, a higher nitrogen concentration in the grown crystal than that of the underlying seed crystal would give rise to misfit strain between the grown crystal and the seed. However, in this case, the sign of the misfit strain is opposite to that having caused the BPD networks; the nitrogen enrichment in the grown crystal results in a smaller lattice constant within the basal plane at the PVT growth temperature ( $\sim 2300^\circ\text{C}$ ), yielding BPDs with extra half-planes pointing in the growth direction when the misfit strain is relieved. This is contradictory to the result of the HRXRD measurements.

Another possible origin of the misfit strain at the grown-crystal/seed interface is the temperature gradient at the interface. Usually, during SiC PVT growth, a positive temperature gradient in the growth direction is set in the growth zone by placing the growth crucible asymmetrically in the radio-frequency (RF) induction coil or the heating furnace (see Figures 1.1a and 1.18a). In addition to this intentionally imposed temperature gradient, the latent heat dissipation associated with the condensation of Si- and C-bearing species sublimed from the source powder would result in an enhanced positive temperature gradient during PVT growth. In this respect, note that SiC has an extremely large latent heat of phase transition from the vapor to the solid (heat of condensation/sublimation), which is estimated to be 580 kJ/mol [44] and more than 10 times larger than that of Si solidification from the melt (50.6 kJ/mol) [45].

With respect to the heating due to the latent heat, another important factor that should be considered is the thickness of the grown crystal in the initial stage of growth. Figure 1.18 explains schematically how the thickness of the grown crystal affects the dissipation of latent heat. Upon condensation of the Si- and C-bearing species, the latent heat is released on the growing crystal surface. The seed crystal is usually placed on a graphite holder, which has a much lower thermal conductivity than that of 4H-SiC at the PVT growth temperature. In the initial stage of PVT growth, the SiC crystal (seed crystal plus grown crystal) is very thin, and thus, all the heat generated by the condensation of Si- and C-bearing species must be dissipated through the backside of the seed crystal (Figure 1.18d). However, the low thermal conductivity of the graphite seed holder means that the generated heat is not dissipated efficiently, and thus, an even larger positive temperature gradient is established at the growing crystal surface during the initial stage of PVT

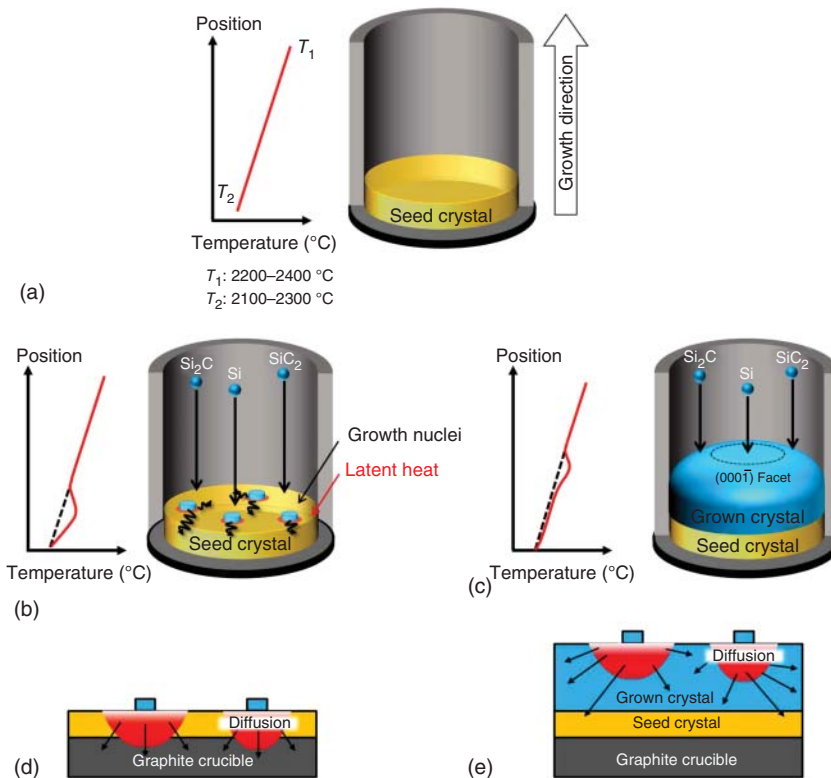


**Figure 1.18** Schematics of latent heat dissipation during PVT growth of 4H-SiC crystals. (a) Positive temperature gradient in the growth direction imposed intentionally in the growth crucible by placing it asymmetrically in the RF induction coil or the heating furnace. (b) Enhancement of temperature gradient at growth front of the grown crystal caused by the poor latent heat dissipation in the initial stage of PVT growth because of the low thermal conductivity of the graphite seed holder; this effect is shown schematically in (d). (c) Case of a thick grown crystal after sufficient time of crystal growth; the enhanced temperature gradient at the growth front is lessened considerably because the generated latent heat can be dissipated efficiently through the thickly grown SiC crystal, as shown schematically in (e).

growth (Figure 1.18b). This large positive temperature gradient causes a large misfit strain within the basal plane at and near the grown-crystal/seed interface, which is relieved by the introduction of BPDs during growth. By contrast, as the grown crystal becomes thicker as it grows, the latent heat is dissipated more efficiently through the body of the thick grown crystal (Figure 1.18e). This lessens considerably the enhanced temperature gradient at the growth front due to the condensation of the Si- and C-bearing species (Figure 1.18c).

The aforementioned strain generation and relaxation processes due to the latent heat are illustrated schematically in Figure 1.19. The figure depicts sequentially (a) the seed crystal prior to PVT growth, (b) the basal plane bending associated with the large temperature gradient in the initial stage of growth, which occurs in a convex manner in the growth direction, (c) the introduction of BPDs to relieve the

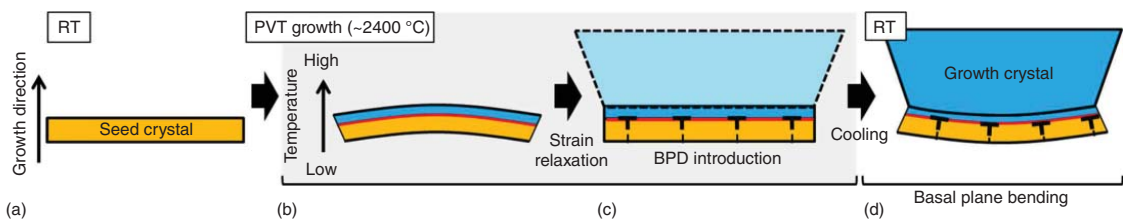


**Figure 1.19** Schematic of introduction of BPDs at grown-crystal/seed interface during PVT growth process, and the resulting basal plane bending after the growth process. Source: Shioura et al. [39]. © 2019, Elsevier; (a) seed crystal prior to PVT growth, (b) basal plane bending associated the large temperature gradient at the initial stage of growth, which occurs in a convex manner toward the growth direction, (c) introduction of BPDs to relax the misfit strain within the basal plane at the grown-crystal/seed interface, and (d) concave-shape basal plane bending toward the growth direction after cooling to room temperature.

misfit strain within the basal plane at the grown-crystal/seed interface, and (d) the resultant concave-shaped basal plane bending in the growth direction after PVT growth. The large basal plane bending due to the poor heat dissipation in the initial stage of PVT growth of SiC was observed experimentally by Hock et al. using in situ X-ray diffraction [46]. They found that the degree of basal plane bending increased with the growth rate, implying that the latent heating due to the condensation of source gas species plays an important role in the basal plane bending in the initial stage of PVT growth.

The final concave shape of the basal plane in the growth direction shown in Figure 1.19d is consistent with the lattice bending observed by HRXRD, and thus, the large positive temperature gradient established at the growing crystal surface during the initial stage of PVT growth would be the most plausible cause of the observed BPD networks. The relationship between the observed BPD networks and the formation of threading dislocations in the initial stage of PVT growth [10–12] is yet to be clarified. However, in Figure 1.17, in addition to the BPD networks, dot-like features are also observed at the nodes of the BPD networks. They are likely to correspond to threading dislocations and suggest that the BPD networks are related closely to them and would be an important source of threading dislocations in PVT-grown 4H-SiC crystals.

As revealed in Figure 1.16, the BPD networks extended fairly deeply in the seed crystal. The maximum depth of the networks in the seed crystal can be estimated from their positions on the surface of the  $1.5^\circ$  off-oriented (000 $\bar{1}$ ) wafer; the networks extended up to 7 mm on the wafer surface from the grown-crystal/seed interface toward the backside of the seed crystal. The distance of 7 mm on the wafer surface corresponds to a depth of 300  $\mu\text{m}$  from the grown-crystal/seed interface toward the backside of the seed crystal. In the initial stage of PVT growth, growth islands are likely to nucleate on the seed crystal surface and then coalesce as the crystal growth proceeds (see Figure 1.18b). Under a large positive temperature gradient, the growth islands tend to incorporate BPDs to relieve the misfit strain due to the temperature gradient, and when the islands coalesce, the BPDs are rearranged and form networks at the grown-crystal/seed interface. The results obtained by Shioura et al. indicated that these BPD networks at the interface were accompanied by extra half-planes pointing toward the backside of the seed crystal and caused the (0001) basal plane to bend in a concave manner in the growth direction after the PVT growth process [39]. An important question here is how and why these BPD networks migrated into the seed crystal during PVT growth.

There are two possible mechanisms for the migration of the BPD networks into the seed crystal, namely, (i) the glide motion of BPDs on the basal plane and (ii) the climb motion of BPDs across the basal plane. To clarify the mechanism for BPD migration into the seed crystal during PVT growth, Shioura et al. conducted a masked PVT growth experiment on a  $4^\circ$  off-oriented (000 $\bar{1}$ ) seed crystal [39]. The result is shown in Figure 1.20, where a reflection X-ray topograph for the diffraction condition  $\mathbf{g} = 11\bar{2}8$  acquired from the boundary area between the masked and unmasked regions of the seed crystal is shown. The masked region (right-hand side of the figure) was covered with a graphite plate during PVT growth to prevent

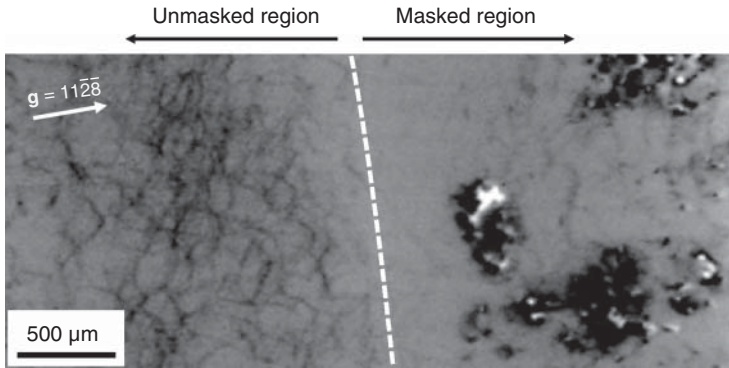


**Figure 1.20** Enlarged reflection X-ray topograph for diffraction condition  $g = 11\bar{2}\bar{8}$  acquired from the boundary area between the masked and unmasked regions of the seed crystal; the 4H-SiC crystal was grown on the unmasked region (left-hand side of the dashed line in the topograph), whereas no crystal growth occurred on the masked region (right-hand side of the dashed line). The topograph shows clearly that the BPD networks in the seed crystal existed only in the unmasked region of the seed crystal. Source: Shioura et al. [39].

crystal growth. As shown in the figure, BPD networks exist only in the unmasked region and do not extend into the masked region. This result shows clearly that the observed BPD networks migrated into the seed crystal through the climb motion of dislocations, as schematically illustrated in Figure 1.21, rather than the glide motion. This is because, had the glide motion been the dominant mechanism for BPD migration, then the BPD networks formed during the initial stage of PVT growth should have glided on the basal plane into the masked region beyond the boundary between the unmasked and masked regions and then been observed in the masked region of the seed crystal after the crystal growth.

The climb motion of dislocations is driven by the injection, diffusion, and incorporation of intrinsic point defects, such as vacancies and interstitials, to the dislocations [47]. As described in Section 1.3.3, the observed BPD networks were accompanied by extra half-planes pointing toward the backside of the seed crystal, and thus, their migration toward the backside of the seed crystal requires vacancies to be incorporated in the dislocations as illustrated schematically in Figure 1.20. Given the migration depth of the BPD networks, it is clear that a large number of vacancies were injected during the initial stage of PVT growth. The mechanism for this remains unclear, but the poor dissipation of the latent heat in the initial stage of PVT growth (see Figure 1.18b,d) would cause local heating of the growing crystal surface, which may induce the injection of a large number of vacancies into the growing crystal.

## 1.4 Conclusions

SiC is a promising material for the next generation of power semiconductor devices, and the adoption of SiC power devices is critical for enabling faster, smaller, lighter,

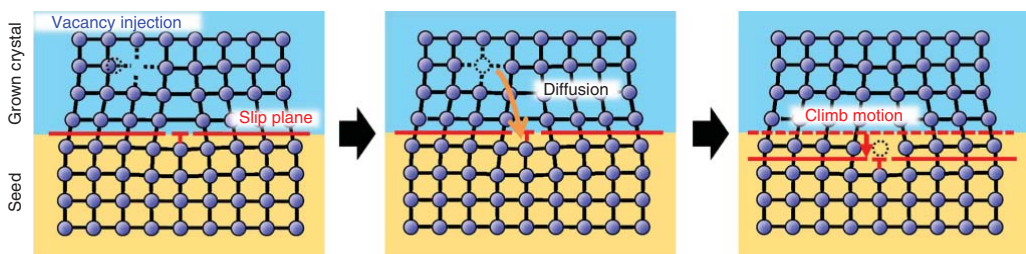


**Figure 1.21** Schematic of the climb motion of a BPD toward the backside of the seed crystal due to the vacancy injection into the growing crystal during PVT growth. Source: Shioura et al. [39]. © 2019, Elsevier.

and more powerful power electronic systems. However, it is amply clear that such a successful adoption of SiC power devices for a wide range of power electronics systems relies considerably on establishing the manufacturing technology for large-diameter high-quality SiC single crystals. This chapter described recent progress in understanding the dislocation formation processes in PVT-grown SiC crystals, which is essential for obtaining high-quality SiC crystals.

After a brief introduction (Section 1.1), Section 1.2 was dedicated to understanding the BPD nucleation and multiplication processes during the PVT growth of 4H-SiC crystals. A large number of BPDs are introduced from the shoulder region of the growth front of 4H-SiC crystals, where a large thermoelastic shear stress is thought to be imposed during PVT growth. Detailed investigations of the BPD distribution in grown crystals suggest that BPDs nucleated at the shoulder region of a growing crystal largely determine the BPD distribution across the entire crystal.

In Section 1.3, the defect structure at the grown-crystal/seed interface of PVT-grown 4H-SiC crystals was investigated using 4H-SiC wafers with a beveled interface between the grown crystal and seed crystal. The existence of BPD networks at the grown-crystal/seed interface was revealed, and they extended considerably into the seed crystal. Such networks were likely to be caused by a large positive temperature gradient imposed on the growing crystal surface because of the local heating by the latent heat dissipation associated with the condensation of Si- and C-bearing species from the vapor during the initial stage of PVT growth. It was also revealed by masked-growth experiments that the migration of the BPD networks deep into the seed crystal was caused by the injection of a large number of vacancies during the initial stage of PVT growth of 4H-SiC crystals.

## References

- 1 Kimoto, T. and Cooper, J.A. (2014). *Fundamentals of Silicon Carbide Technology: Growth, Characterization, Devices, and Applications*. Singapore: Wiley.
- 2 Tairov, Yu.M. and Tsvetkov, V.F. (1978). *J. Cryst. Growth* 43: 209.
- 3 Wahab, Q., Ellison, A., Henry, A. et al. (2000). *Appl. Phys. Lett.* 76: 2725.
- 4 Fujiwara, H., Naruoka, H., Konishi, M. et al. (2012). *Appl. Phys. Lett.* 100: 242102.
- 5 Yamamoto, K., Nagaya, M., Watanabe, H. et al. (2012). *Mater. Sci. Forum* 717–720: 477.
- 6 Agarwal, A., Fatima, H., Haney, S., and Sei-Hyung, R. (2007). *IEEE Electron Device Lett.* 28: 587.
- 7 Veliadis, V., Hearne, H., Stewart, E.J. et al. (2012). *IEEE Electron Device Lett.* 33: 952.
- 8 Bergman, P., Lendenmann, H., Nilsson, P.A. et al. (2001). *Mater. Sci. Forum* 353–356: 299.
- 9 Lendenmann, H., Dahquist, F., Johansson, N. et al. (2001). *Mater. Sci. Forum* 353–356: 727.
- 10 Takahashi, J., Ohtani, N., and Kanaya, M. (1996). *J. Cryst. Growth* 167: 596.

- 11 Sanchez, E.K., Liu, J.Q., De Graef, M. et al. (2002). *J. Appl. Phys.* 91: 1143.
- 12 Suo, H., Tsukimoto, S., Eto, K. et al. (2018). *Jpn. J. Appl. Phys.* 57: 065501.
- 13 Hobgood, H.McD, Brady, M.F., Brixius, W.H. et al. (2000). *Mater. Sci. Forum* 338–342: 3.
- 14 Selder, M., Kadinski, L., Durst, F., and Hofmann, D. (2001). *J. Cryst. Growth* 226: 501.
- 15 Ma, R.-H., Zhang, H., Dudley, M., and Prasad, V. (2003). *J. Cryst. Growth* 258: 318.
- 16 Gao, B. and Kakimoto, T. (2014). *Cryst. Growth Des.* 14: 1272.
- 17 Herro, Z.G., Epelbaum, B.M., Bickermann, M. et al. (2004). *J. Cryst. Growth* 262: 105.
- 18 Yamaguchi, T., Ohtomo, K., Sato, S. et al. (2015). *J. Cryst. Growth* 431: 24.
- 19 Pons, M., Madar, R., and Billon, T. (2003). *Silicon Carbide – Recent Major Advances* (eds. W.J. Choyke, H. Matsunami and G. Pensl), 121–136. Berlin: Springer.
- 20 Powell, A.R., Leonard, R.T., Brady, M.F. et al. (2004). *Mater. Sci. Forum* 457–460: 41.
- 21 Tymicki, E., Graszka, K., Diduszko, R. et al. (2007). *Cryst. Res. Technol.* 42: 1232.
- 22 Ohtani, N., Ohshige, C., Katsuno, M. et al. (2014). *J. Cryst. Growth* 386: 9.
- 23 Ohshige, C., Takahashi, T., Ohtani, N. et al. (2014). *J. Cryst. Growth* 408: 1.
- 24 Tani, K., Fujimoto, T., Kamei, K. et al. (2016). *Mater. Sci. Forum* 858: 73.
- 25 Straubinger, T.L., Bickermann, M., Weingärtner, R. et al. (2002). *J. Cryst. Growth* 240: 117.
- 26 Nakano, T., Shinagawa, N., Yabu, M., and Ohtani, N. (2019). *J. Cryst. Growth* 516: 51.
- 27 Sonoda, M., Nakano, T., Shioura, K. et al. (2018). *J. Cryst. Growth* 499: 24.
- 28 Wang, S., Dudley, M., Carter, C. Jr., et al. (1993). *Mater. Res. Soc. Symp. Proc.* 307: 249.
- 29 Zhang, X., Ha, S., Hanlumnyang, Y. et al. (2007). *J. Appl. Phys.* 101: 053517.
- 30 Hirth, J.P. and Lothe, J. (1982). *Theory of Dislocations*, 2e, 63. New York: Wiley.
- 31 Ha, S., Mieszkowski, M., Skowronski, M., and Rowland, L.B. (2002). *J. Cryst. Growth* 244: 257.
- 32 Ohtani, N., Katsuno, M., Tsuge, H. et al. (2006). *Jpn. J. Appl. Phys.* 45: 1738.
- 33 Powell, A.R., Sumakeris, J.J., Khlebnikov, Y. et al. (2016). *Mater. Sci. Forum* 858: 5.
- 34 Nakashima, S. and Harima, H. (1997). *Phys. Status Solidi A* 162: 39.
- 35 Sugie, R. and Uchida, T. (2017). *J. Appl. Phys.* 122: 195703.
- 36 Sakakima, H., Takamoto, S., Murakami, Y. et al. (2018). *Jpn. J. Appl. Phys.* 57: 106602.
- 37 Ohtani, N., Katsuno, M., Fujimoto, T. et al. (2009). *Jpn. J. Appl. Phys.* 48: 065503.
- 38 Chen, Y., Dhanaraj, G., Dudley, M. et al. (2006). *Mater. Res. Soc. Symp. Proc.* 911: 151.
- 39 Shioura, K., Shinagawa, N., Izawa, T., and Ohtani, N. (2019). *J. Cryst. Growth* 515: 58.
- 40 Yugami, H., Nakashima, S., Mitsuishi, A. et al. (1987). *J. Appl. Phys.* 61: 354.

- 41 Nakashima, S., Harima, H., Ohtani, N., and Katsuno, M. (2004). *J. Appl. Phys.* 95: 3547.
- 42 Matsumoto, T., Nishizawa, S., and Yamasaki, S. (2010). *Mater. Sci. Forum* 645–648: 247.
- 43 Sasaki, S., Suda, J., and Kimoto, T. (2012). *Mater. Sci. Forum* 717–720: 481.
- 44 Drowart, J., de Maria, G., and Inghram, M.G. (1958). *J. Chem. Phys.* 29: 1015.
- 45 Dold, P. (2015). *Advances in Photovoltaics: Part 4, Semiconductors and Semimetals*, vol. 92 (eds. G.P. Willeke and E.R. Weber), 13. Waltham, MA: Academic Press.
- 46 Hock, R., Konias, K., Perdicaro, L. et al. (2010). *Mater. Sci. Forum* 645–648: 29.
- 47 Hull, D. and Bacon, D.J. (1984). *Introduction to Dislocations*, 3e, 58. Oxford: Pergamon Press.

## 2

### Industrial Perspectives of SiC Bulk Growth

*Adrian R. Powell*

*Cree, Inc., 4600 Silicon Drive, Durham, NC 27703, USA*

#### 2.1 Introduction

In this chapter, we discuss the inherent differences between growing SiC wafers for specialized high-end niche markets and the production of SiC wafers substrates for large-volume manufacturing. Both are critical in developing a robust commercial market. In the case of SiC, many academic and industrial players have contributed to the impressive ramp in quality and diameter that SiC wafers have experienced over the last 30 years. Figure 2.1 shows how the maximum diameter of SiC wafers has increased since the first commercial release in 1991 along with some of the critical milestones [1–4].

Currently, there are three primary markets for SiC wafers: (i) low-doped substrates for GaN light-emitting diode (LED) structures, (ii) high-doped substrates for high-power SiC device structures, and (iii) semi-insulating substrates for high-frequency GaN devices. In the following sections, we will discuss the commercial needs of each of these in turn. For each, we will address the key question of price vs. quality. For commercialization, it is important to remember that the perfect substrate is the one that meets all the customer needs at the lowest cost to produce. It is this balance between providing substrates that meet all customer requirements and are priced as low as possible that distinguishes industrial development from academic research.

#### 2.2 SiC Substrates for GaN LEDs

The first high-volume usage of SiC substrates was driven by the release of high-brightness blue and green LEDs in the early 2000s by both Cree and Osram. This was the product that took the production of SiC substrates into true commercialization. GaN LEDs are fabricated on SiC substrates through heteroepitaxy. The unit cells and thermal expansion of SiC and GaN are not perfectly matched;

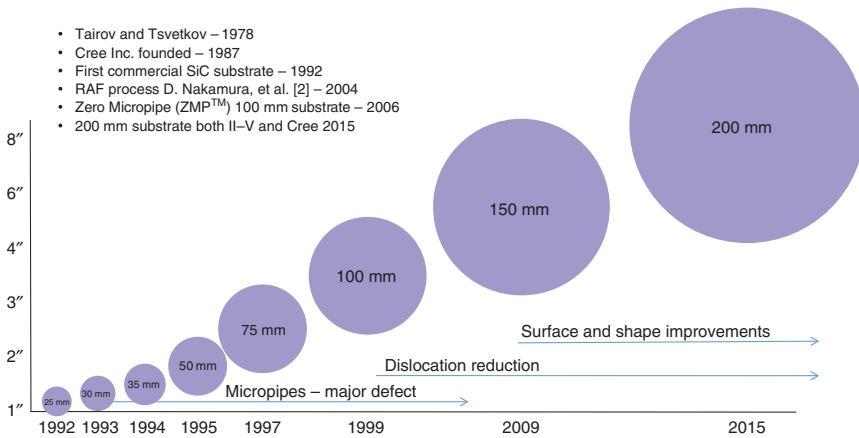


**Figure 2.1** Progression of demonstrated single-crystal wafer diameter.

however, the match is superior to other available substrates (Si or Sapphire), and the nucleation of high-quality GaN layers can be achieved.

The primary factor that controls this nucleation is the offcut angle of the substrate. Thus, tight tolerances to  $<0.25^\circ$  are required here, and any curvature of the lattice planes within the substrate must be avoided. However, even with optimal nucleation conditions, the interface between SiC and GaN introduces many, typically greater than  $10^5 \text{ cm}^{-2}$  dislocations [5, 6], which are subsequently controlled by complex buffer structures in the GaN epitaxial growth. The consequence of this for the SiC substrate manufacturer is that dislocation densities in the substrates become non-critical at substrate values below  $10^5 \text{ cm}^{-2}$ . The final critical parameter for LED substrates is their optical characteristics. Many of the LED chip structures rely upon the generated light traveling through the substrate and therefore a transparent substrate is desired, this in turn defines a purity level required. In the case of SiC, the most problematic impurities are nitrogen, boron, and aluminum. Since all three of these are electrically active and cause absorption of the light emitted by the LED, in general the level of impurities in the substrates must be kept below  $10^{17} \text{ cm}^{-3}$ . In the most recent decade, the ability to produce these LED diode structures on Sapphire substrates has improved, and so it is anticipated that further market growth of this segment will be static due to the lower price point of Sapphire substrates.

### 2.3 SiC Substrates for Power SiC Devices

LEDs allowed the first commercialization of SiC substrates; however, as we enter the next decade, it is expected that the volume of the power product will expand. In 2019, over 1 billion dollars of expansion was announced by various SiC substrate manufacturers mostly directed toward power device structures. SiC power devices include Schottky and MOSFET diodes. These devices are fabricated in SiC epitaxy grown directly on SiC substrates. For SiC epitaxy, the growth is carried out on

4° offcut surfaces, and this in turn reduces the requirement for very low lattice plane curvature. However, the quality requirements of the epitaxial SiC on SiC substrates are extremely high, and therefore, any defects in the substrate that thread into the epitaxy are a great concern. This leads to stringent limits on defect densities in the substrate with micropipes typically below  $1 \text{ cm}^{-2}$  and dislocations  $<10^3 \text{ cm}^{-2}$ . Unlike LEDs, these device structures electrically connect through the substrate requiring highly doped, low resistivity material. Generally, nitrogen is the active dopant, and resistivity values are desired to be as low as possible (0.015–0.028  $\Omega\text{-cm}$ ) so as to minimize device on resistance. It is known that a higher doping concentration leads to the occurrence of stacking fault defects in the active devices [7] and so this sets the minimum wafer resistivity.

## 2.4 SiC Substrates for High-Frequency Devices

High-frequency power devices are made from GaN on SiC; consequentially, the demands are similar to those of LED structures with the additional requirement that the substrate must not electrically couple to the active device. Thus, a very high resistivity substrate is desired. This can be achieved either through the addition of a deep level impurity such as vanadium [8] or by reducing the level of all impurities to a level less than  $2 \times 10^{-16} \text{ cm}^{-3}$  [9]. Table 2.1 shows the key aspects of substrate quality that must be present to allow high-yielding stable device structures to be manufactured for all three product types.

## 2.5 Cost Considerations for Commercial Production of SiC

The basic wafer supplier question is “how to provide high quality wafers, at a minimal cost.” For SiC, that means that the manufacturer must consider where the

**Table 2.1** Indicating substrate characteristics beyond which significant final device yield hits might be expected<sup>a)</sup>.

Characteristic	LED (GaN on SiC)	Power (SiC on SiC)	High frequency (GaN on SiC)
Surface orientation	$0.0 \pm 0.25$	$4.0 \pm 0.5$	$0.0 \pm 0.25$
Micropipe density	$<5 \text{ cm}^{-2}$	$<1 \text{ cm}^{-2}$	$<1 \text{ cm}^{-2}$
Basal plane	$<10^5 \text{ cm}^{-2}$	$<10^3 \text{ cm}^{-2}$	$<10^5 \text{ cm}^{-2}$
Threading screw	$<10^5 \text{ cm}^{-2}$	$<10^3 \text{ cm}^{-2}$	$<10^5 \text{ cm}^{-2}$
Threading edge	$<10^5 \text{ cm}^{-2}$	$<10^5 \text{ cm}^{-2}$	$<10^5 \text{ cm}^{-2}$
Resistivity	$>0.2 \Omega\text{-cm}$	$0.015 < x < 0.03 \Omega\text{-cm}$	$>10^5 \Omega\text{-cm}$

a) Commercial specs are often set well inside these limits.

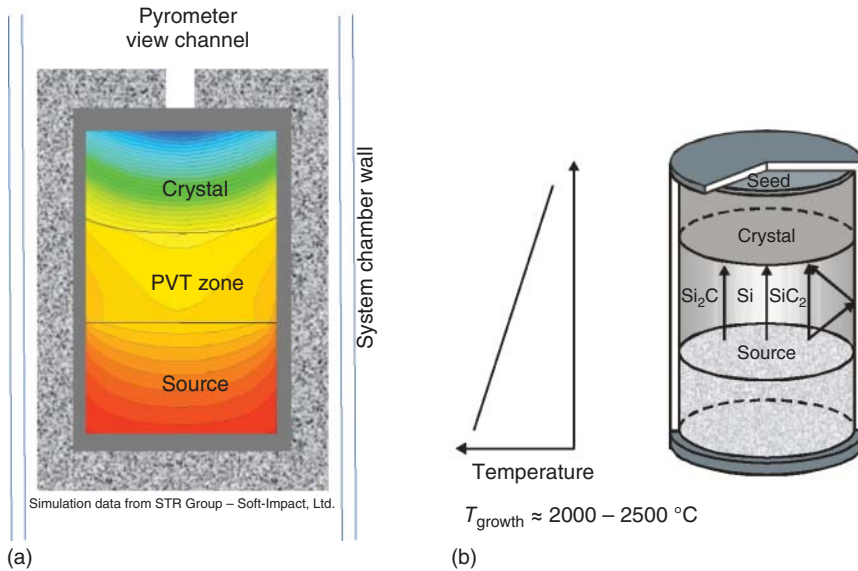


**Figure 2.2** (a) Schematic of a SiC growth system, (b) schematic of gases present during growth. Source: Tairov and Tsvetkov [1].

main cost drivers are in the process and reduce them. Currently, in 2020, virtually all commercial SiC production utilizes the modified Lely technique, shown in Figure 2.2. Here, a seed wafer of SiC is placed at the top of the crucible and SiC source material placed at the base. The crucible is then heated to temperatures in excess of  $2000 \text{ }^\circ\text{C}$ . The overall temperature is controlled by pyrometer feedback to the power supply, and the thermal field shape is controlled both by the positioning of the thermal insulation and by where the heat energy is coupled into the crucible. In a typical growth, both the absolute temperature and the axial thermal gradient are adjusted to maintain optimal thermal fields. As the seed/crystal region is kept cooler than the source region, the SiC sublimation gases sublime from the source and condense on the growing crystal.

From a cost point of view, we have several items to consider and these are outlined in Table 2.2.

## 2.6 Raw Materials

For modified Lely growth, one requires a seed of similar diameter to the final grown crystal. This of course has a cost similar to that of a completed SiC wafer. In this style of growth (unlike Si growth), there is no necking down of the crystal diameter, and therefore, any threading defects or misoriented regions in the seed wafer will be propagated into the growing crystal. This difficulty in producing crystals with significantly larger diameter than the seed used is one of the factors that has slowed the increase in SiC wafer diameter available to the commercial market. Two main approaches have been used for seed diameter expansion; the

**Table 2.2** Cost considerations for SiC bulk growth.

Requirement	Subsystem	Cost is a function of
Raw materials	Seed, SiC source material	Part purity and efficiency of conversion to final crystal
Reactor hot zone Equipment	Graphite crucible, insulation Crystal growth system	Part purity, part size, part lifetime Time required for growth process (turns per year)
Wafer manufacture	Wafering and polish	Equipment cost and throughput, slurry cost
Yield	Fraction of high-quality product per start	Bulk crystallographic defects, boules and processing machining errors, kerf loss, and wafer thickness

first is a gradual increase in crystal diameter, here the region of high-quality crystal is expanded, growth after growth, where the general orientation of the growth direction is in the “*c*” axis direction, an example of a 2” to 2.75” diameter expansion was shown by II-VI Inc. [10] (Figure 2.3a), and the second approach was pioneered by Denso Inc. [2] and termed “Repeated A Face” growth (Figure 2.3b). In this second approach, a crystal is first grown on the “*c*” axis direction; however, instead of slicing perpendicularly to the “*c*” axis, an orthogonal slice is taken perpendicular to the  $(1\bar{1}00)$  plane, this slice is used as a seed to grow a second crystal in the  $\langle 1\bar{1}00 \rangle$  direction, from which an orthogonal slice is also taken, this time allowing growth in the  $\langle 11\bar{2}0 \rangle$  direction, again this slice is then used to grow a crystal and an orthogonal slice taken, this time the slice is perpendicular to the  $\langle 000\bar{1} \rangle$  direction and it is suitable to be a seed for a conventional growth, and thus a high-quality *c*-axis seed boules can be produced. It should be noted that due to the challenges involved in creating high-quality seeds, many manufacturers place restrictions on their wafer sales, preventing the use of a commercially sold wafer as a seed substitute.

The other primary input is the source material; in the modified Lely process, this is SiC powder, and the key cost parameter here is what fraction of powder is transported to grow the crystal, rather than to create parasitic deposits elsewhere in the crucible, gas leakage out of the crucible, or simply residual source not consumed during growth.

## 2.7 Reactor Hot Zone

The modified Lely approach for SiC is unusual compared to other commercial crystal growth processes in that it operates at very high temperatures 2200–2400 °C [11, 12]. At these temperatures, there is a limited pallet of materials available that (i) withstand the temperature without decomposing and (ii) can be fabricated at high purity levels. The most commonly used material for both crucible and insulation is graphite. Figure 2.2a shows a typical reactor configuration for the hot zone showing

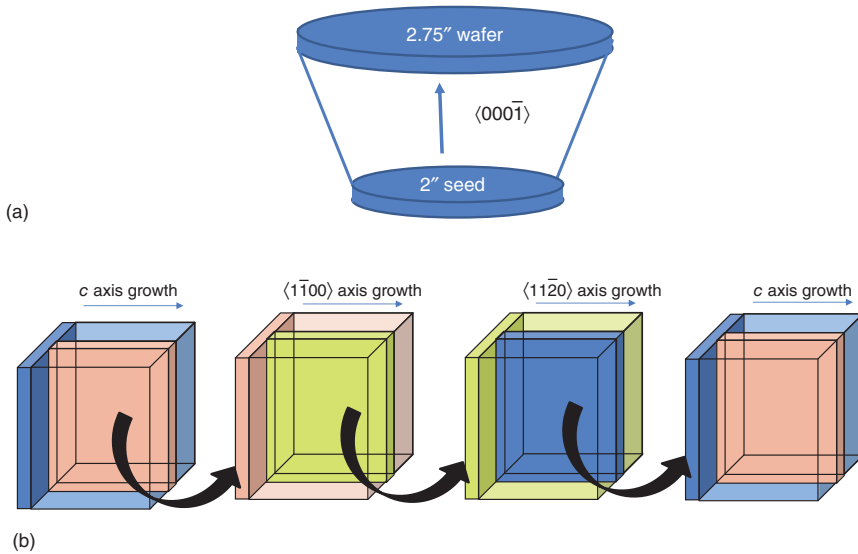


**Figure 2.3** Two differing methods for expanding SiC seed: (a) schematic of gradual expansion and (b) schematic of repeated A-face growth (RAF) technique.

(i) crystal location, (ii) source location, (iii) crucible walls, (iv) insulation materials, and (v) reactor walls.

The challenge with graphite for the crucible build at these high growth temperatures, and in the presence of typical gases Si, Si<sub>2</sub>C, and SiC<sub>2</sub>, is that serious etching can occur on the inside walls of the crucible. It is key that the crucible remains whole for the entirety of the growth process. This etching behavior is enhanced at higher temperatures, again leading to a compromise choice between costs in terms of crucible parts lifetime vs. the savings achieved through increasing the growth rate by increasing growth temperatures.

Next out from the crucible is the insulation package that serves two major functions. The first of these is to keep the heat in the hot zone, to avoid high power consumption levels, without any insulation; the simple crucible shown in Figure 2.2a would need about 700 kW to maintain its temperature, this would not be financially viable. The second function is to allow control of the thermal profile within the growth crucible, by variation of the thickness and thermal properties of the insulating material surrounding that crucible. For example, it can be seen in Figure 2.2a that the gap in the insulation at the top of the crucible provides both a clear path for temperature control via a pyrometer and an exit route for energy in the crucible. This in turn locally cools the crystal directly below the “pyrometer view channel,” thus providing a concave thermal field in the crystal region. Since SiC will deposit preferentially at the coolest location, this configuration would be expected to grow a convex SiC crystal as suggested by the schematic.

As one moves away from the hot zone, other more standard insulation materials become more viable, and the system design tends toward more standard low-pressure grower designs.

## 2.8 System Equipment

Many SiC wafer vendors keep their reactor geometry proprietary, though some early images are available [13]; in addition, there are currently several commercial vendors of SiC furnaces. However, whatever the source of the reactor, the cost of ownership is high and the factory floor space requirement is substantial. As an example, consider a published growth rate of 0.1 mm/h [14]. Assuming very effective reactor turn around, one might then grow 800 mm of crystal in a year from this grower. If one then assumes a US\$ 1 million grower cost, a five-year depreciation, and excellent yields, a typical wafer slice would have a contributory cost of over US\$ 200 from the grower equipment alone. This high cost drives the desire to increase the SiC growth rate. However, as the growth rate is pushed up, there is a tradeoff between high growth rates and induced crystalline defects. This will be discussed in the following section.

## 2.9 Yield

Left till last, but as in all processes, the yield is of immense importance. The cost of growing a defective crystal is the same as that of growing a high-quality crystal, so we must ensure that our growth process creates few defective crystals. Unfortunately, the need to produce a high-growth-rate, long-length crystal from a low-cost starting set of raw materials is often in direct competition to growing low defectivity crystals. The science of production is to create the optimal balance between these competing factors. Figure 2.4 shows many of the defects associated with the growth of SiC boules. Some of these have been well characterized by the scientific community and the mechanisms of their formation well understood. However, the nucleation mechanisms of others are still not fully explained, and much exciting work remains in the field to identify root causes and optimal ways to prevent the defect formation in standard growths.

The creation of a new product or process requires several stages – each with a unique focus. Originating in research phase, where researchers champion the few excellent crystals to highlight where the process can go, the process typically moves through to early production where the focus changes to how to increase the total number of passing wafers, i.e. yield enhancement. From there, the process typically moves on to full production, where reducing process cost is of primary concern. For SiC, this yield and cost improvement is generally split into three categories: (i) Reduction of total failures: typical causes of these are equipment failure and nucleation of differing polytypes and orientations near the start of growth (Figure 2.4a,d,f). (ii) Reduction of mid boule fails: typical causes are incorporation of particles and local switching of polytype (Figure 2.4c,e). (iii) Finally, overall tightening of slicing and surface finish processes help to boost the yield to acceptable levels.

As the understanding of how the input materials, and process variables, effect the different fail modes, the overall process yield can be continually increased whilst simultaneously allowing some loosening of non-key input specifications to allow for lower cost inputs.

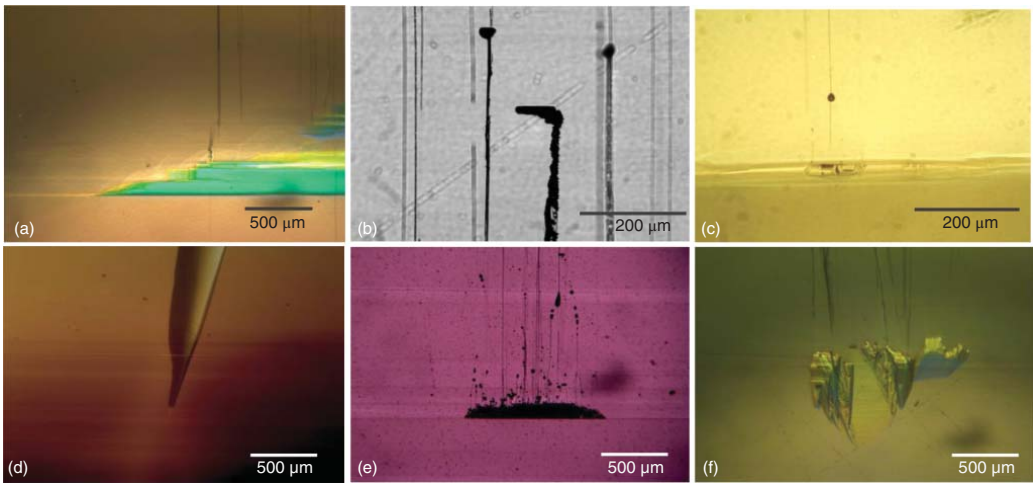
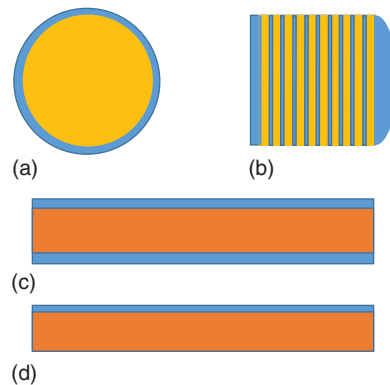


**Figure 2.4** Images of six defect modes that are commonly observed in SiC growth, in all cases the growth direction is upward. (a) Polytotype switch from 4H, to 6H, 15R, and back, (b) large voids migrating through the crystal, (c) defect inclusion generating a small tear-shaped void, (d) initiation point of an inclusion of different orientation of SiC, (e) large growth disruption introducing many pipes and dislocations, (f) 3C inclusion, here some of the side facets of the 3C inclusion are clearly visible with the center region showing a characteristic yellow color.

**Figure 2.5** Schematic illustrating overall kerf loss for wafer manufacture processes, (a) OD grind loss from outer perimeter, (b) saw loss, (c) loss in double side polish, and (d) loss in final single side CMP.



## 2.10 Turning Boules into Wafers

Once a SiC boule has been grown, it must then be converted into high-quality wafers. For SiC, there are challenges here due to its high hardness value of 9.4 Mohs and general chemical inertness. The general process is as follows:

- (a) Grind the crystal down to the desired diameter
- (b) Slice this boule into wafers
- (c) Mark the wafers with identification, orientation flats, and appropriate edge shape
- (d) Rough polish the wafers
- (e) Final chemical mechanical polish (CMP) step
- (f) Characterize and supply to customer

From a cost point of view, it is worth considering that each processing step removes SiC crystal and thus represents a kerf loss. Typical kerf loss mechanisms and values are shown in Figure 2.5: Outer diameter (OD) grind 3–10%, seed and dome removal 1–5%, wafer slicing 30–40%, rough double side polish 10–20%, and final CMP <1%. Together, these can easily represent more than half of the grown crystal mass. Kerf loss has a critical role to play in the final cost of SiC wafer product and is particularly hurtful to crystal growers, as it represents the loss of high-quality material to the shaping operations. Much development work has gone into improving processing techniques to reduce overall kerf losses and increase the yield of these processes.

## 2.11 Crystal Grind

This is a fairly typical process for bulk crystal processing, where the SiC crystal is rotated and brought into proximity with a high-speed diamond grind wheel. The diamond cutting teeth on the wheel will then locally scrape away the SiC crystal material; however, SiC is unusual in that for most crystal materials, the local heating caused by the cutting diamond tooth causes the crystal to exceed the ductile to brittle transition temperature. Thus, the material removal is conducted in the

ductile domain where cracking is eliminated. For SiC, since the ductile to brittle transformation is high [15], the grind operation is generally in the brittle domain, and consequently, cracks are initiated at the outer grind surface. Care must be taken to ensure that these cracks do not propagate deeply into the crystal. In practice, to minimize this crack depth, a low grind rate is used, and the final outer edge of the crystal is effectively cleaned up later in the wafer edge grind and polish steps.

## 2.12 Wafer Slicing

Wafer slicing is where the thickness, orientation, and much of the final wafer shape are determined. Over the past two decades, multi-wire slicing has become the dominant process for slicing boules (<http://www.takatori-g.co.jp/english>). In multi-wire slicing, a thin steel wire is coated with a diamond slurry, and this wire is pulled backward and forward across the SiC surface at a speed up to 10 m/s. The process is essentially a lapping process directly between the wire and the SiC surface, with the diamond slurry providing the abrasive material and the wire acting to provide both the downforce and the lateral velocity to the diamond particles. This process creates a trench at each wire location that gradually becomes deeper as the operation continues. This operation is inherently slow since the removal rate for the lapping process is roughly 5 mm/h. Thus, many hours are needed to cut through a 150-mm-diameter boule. To effectively speed up this process, the wire is wrapped around rollers such that a wire web is created with several hundred parallel wires; consequentially, although the slicing process itself is slow, the ability to cut several hundred slices concurrently alleviates this (Figure 2.6).

While this slicing process is simple in concept, many parameters such as wire tension, wire speed, diamond slurry composition, downforce applied to the wire, and wire diameter must be tightly controlled to cut the crystal successfully without imparting excessive shape into the sliced wafers. One further consideration is the need to maintain a stable cutting zone. Effects such as differential temperatures or nonoptimal thermal expansion loops will tend to cause the wires to move sideways during the cut which will often cause displacement of wires w.r.t. the crystal and poor wafer shape particularly at the start and end of a cut where the rapidly changing cut length makes it more difficult to hold slicing conditions stable.

In addition to wafer shape induced by the saw, there is additional shape induced due to both residual stress in the grown crystal and due to differential damage depths on the Si face vs. the C face of the wafers. This tends to impart a radially symmetric shape into the wafer. Figure 2.7 shows how the shape of 150 mm wafers have been improved through the optimization of growth and slicing processes.

There is interest in other slicing techniques predominantly due to the potential of lower kerf loss. These include laser splitting [16], electrical discharge machining (EDM) [17] slicing, and diamond impregnated wire slicing.

Laser splitting utilizes a high-power laser to locally heat a region of the crystal beneath the surface, and this thermal expansion in turn creates microcracks that are predominantly in the basal plane direction. Through careful control, this heating

**Figure 2.6** Schematic showing modern wire saw configuration:

(a) configuration of boule with respect to wire web, (b) cross section of wire coated in slurry cutting crystal, (c) lateral cross section showing slurry velocity causing a rolling motion in the diamond particles. Note for many commercial saws, the wire cuts upward into the crystal as shown in the figure.

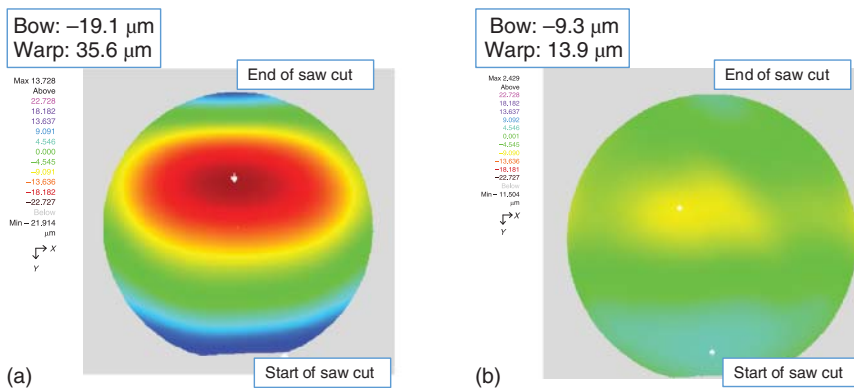
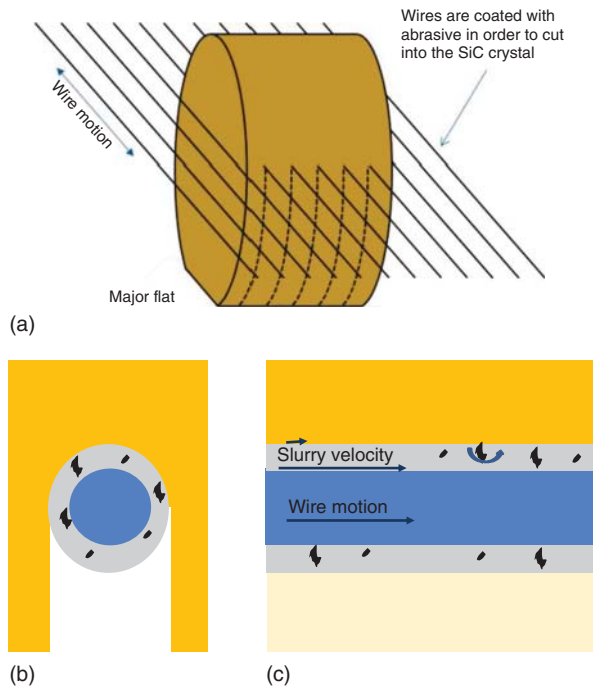


**Figure 2.7** (a) A 150 mm wafer shape obtained from an unoptimized cut, (b) 150 mm wafer shape obtained once slicing parameters are optimized.

can be maintained within a very tight depth window from the surface of the boule, and thereby, as this laser is scanned across the wafer, a “sheet of cracks” can be produced. It then becomes possible to peel or pull this top wafer from the boule. This technique could in principle reduce kerf loss to below 50 μm and is only limited by the accuracy of the optical system controlling the depth of penetration and the degree of localization of the cracking behavior.

EDM slicing is similar to wire slicing except that in this case a high voltage in the wire is used to strike a plasma between the wire and the crystal. This plasma in turn

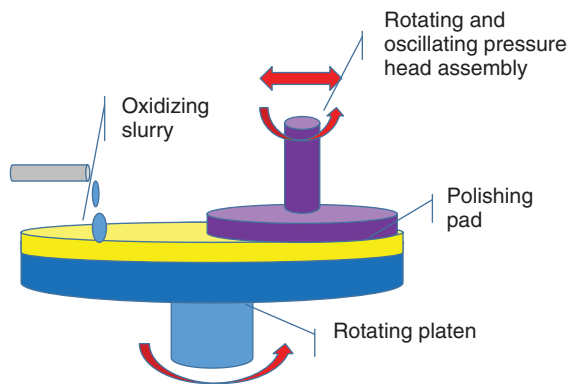


**Figure 2.8** Schematic of a CMP process.

etches the crystal to create the slicing operation. Since the wire is not being required to both carry slurry and provide the downforce, it may be possible to reduce wire diameter significantly and therefore reduce material kerf loss.

Diamond impregnated wire slicing, as oppose to diamond slurry wire slicing, is gaining in popularity due to the potential of reduced wire tension, and thus the reduced diameter wire required, thereby producing reduced kerf loss. As the name implies, this technique is very similar to typical wire slicing, except that the abrasive (diamond) is actually bonded to the wire before the cutting operation.

### 2.13 Wafer Polish

Once the crystals have been sliced into wafers, the processing becomes similar to that of other semiconductors in that a series of surface finishing steps are used that typically consist of polishing with successive steps of abrasive material reducing the abrasive diameter with each step (diamond for SiC wafers). This type of removal will always leave a damaged sublayer in the wafer whose depth is proportional to the abrasive size. Consequentially, the final finish is provided by a CMP step, Figure 2.8, where an oxidizer is combined with a soft abrasive. The oxidizer converts the surface layer of SiC to SiO<sub>2</sub>, and this oxide layer is then removed by the soft abrasive. Fortunately, the soft abrasive is not aggressive enough to scratch SiC, and so a high-quality surface can be achieved.

### 2.14 Summary

Over the last 30 years, SiC materials growth has developed into a mature industry with multiple manufacturers of high-quality wafers who have supplied millions of wafers to the market. This industry has also increased the diameter of these wafers from 25 mm up to as large as 200 mm representing an almost two-order-of-magnitude increase in surface area available for device manufacture on each wafer. Simultaneously, these manufactures have increased the wafer quality